PAPER

# MX family: an efficient platform for topological spintronics based on Rashba and Zeeman-like spin splittings

To cite this article: Majeed Ur Rehman and Zhenhua Qiao 2023 *J. Phys.: Condens. Matter* **51** 015001

IOP Publishing Journal of Physics: Condensed Matter
J. Phys.: Condens. Matter **51** (2023) 015001 (19pp) https://doi.org/10.1088/1361-648X/ac9d15

# MX family: an efficient platform for topological spintronics based on Rashba and Zeeman-like spin splittings

**Majeed Ur Rehman**[1] **and Zhenhua Qiao**[1,2,*]

[1] CAS Key Laboratory of Strongly-Coupled Quantum Matter Physics, and Department of Physics, University of Science and Technology of China, Hefei, Anhui 230026, People's Republic of China
[2] ICQD, Hefei National Research Center for Physical Sciences at Microscale, University of Science and Technology of China, Hefei, Anhui 230026, People's Republic of China

E-mail: qiao@ustc.edu.cn

Received 22 July 2022, revised 3 October 2022
Accepted for publication 24 October 2022
Published 8 November 2022

**Abstract**

Taking various combinations of M = (Mo, W) and X = (C, S, Se) as examples, we propose that MX (M = transition metals, X = IV,V or VI elements) family can establish an excellent platform for both conventional and topological spintronics applications based on anisotropic Rashba-like and non-magnetic Zeeman-type spin splittings with electrically tunable nature. In particular, we observe sizeable Zeeman-like and Rashba-like spin splittings with an anisotropic nature. Meanwhile, they exhibit Rashba-like and topologically robust helical edge states when grown in ferroelectric and paraelectric phases, respectively. These MX monolayers are realized to be quantum valley Hall insulators due to valley contrasting Berry curvatures. The carriers in these MX monolayers can be selectively excited from opposite valleys depending on the polarity of circularly polarized light. The amplitude of the spin splitting can be further tuned by applying external means such as strain, electric field or alloy engineering. Furthermore, considering graphene sheet over the WC monolayer as a prototype example, we show that these MX monolayers can boost the relativistic effect by coupling with the systems exhibiting extremely weak spin–orbit coupling (SOC). Depending on the surface of WC monolayer in contact with the graphene sheet, graphene over WC monolayer passes through the transformation from the semiconducting junction to the Shotcky barrier-free contact. Finally, we reveal that these MX monolayers could also be grown on the substrates such as $WS_2(001)$ and GaTe (001) with type-II band alignment, where electron and hole become layer splitted across the interface. Our analysis should be fairly applied to other systems with strong SOC and an equivalent geometrical structure to the MX monolayers.

Keywords: topological, spintronics, Rashba

(Some figures may appear in colour only in the online journal)

## 1. Introduction

Spintronics utilize the spin degree ptof freedom as a driving force for the information encoding and storing, giving rise to an extensive range of electronic applications, such as magnetic-memories/sensors with low power consumption [1, 2]. In spintronics, spin–orbit coupling (SOC) is the key factor that encouraging all the spin-based phenomena. In this sense, a subclass of two-dimensional materials with strong SOC is very promising for spintronics applications. Similarly, SOC when merge with other degrees of freedom such

* Author to whom any correspondence should be addressed.

 

as valley and magnetism, reveal a spectrum of phenomena including non-magnetic, magnetic and light-controlled topological features [3–7]. The spintronics, which have been realized so far, are limited to the magnetic systems based on the exchange interaction of electrons with local magnetic-moments to generate spin currents. However, the control of the magnetization in such systems typically demands large energies and causes undesired magnetic-fields, preventing high densification of devices. Recently, the SOC has been identified as an alternating promising route to realize the spintronics in non-magnetic materials, where it is relatively accessible to generate spin currents from charge currents and vice versa in a controllable way. The so-called spin Hall effect [8, 9] and inverse spin Hall effect [10], are two examples of these phenomena.

Energy bands remain degenerate with zero spin splitting as long as the time reversal and space inversion symmetries are preserved in the system. The time-reversal and space inversion symmetries impose the constraint $[E^{\uparrow}(k) = E^{\downarrow}(-k)]$ and $[E^{\uparrow}(k) = E^{\uparrow}(-k)]$ on each band, respectively. However, this degeneracy can be lifted by breaking one of the above symmetries. In principle, the spatial inversion symmetry is broken at the surfaces and interfaces of non-magnetic systems. A non-conventional SOC, known as Rashba SOC, exists in such systems [11–13]. This Rashba-like SOC breaks the spin degeneracy in the band structure except at some special $k$-points in the first Brillouin zone where Kramers theorem $[E^{\uparrow}(\mathrm{k}) = E^{\downarrow}(\mathrm{k})]$ holds (see figure 1). These $k$-points in the Brillouin zone are known as time-reversal invariant momenta (TRIM). This type of spin splitting is commonly known as Rashba spin splitting and is highly demandable for spintronics applications ranging from quantum computing, topological matter, and cold atom systems [14–16].

Generally, Rashba SOC is odd in momentum $k$ for system with broken inversion symmetry, which reduces to a linear dependence in the simplest two-dimensional free electron approximation, and is described by the Hamiltonian $H_R = \alpha_R \hat{\sigma}.(\hat{k}_{\parallel} \times \hat{e_z})$, where $\alpha_R$, $\hat{k}_{\parallel}[= (k_x, k_y, 0)]$, and $\hat{\sigma}$ represent the strength of the Rashba SOC, qausi-momentum in the plane of two-dimensional system and set of pauli matrices in the spin-space, respectively [11]. In principle, Rashba SOC mixes the up and down spin components and thus $s_z$ remains no more a good quantum number. So far, the Rashba SOC has been observed in many two-dimensional systems including graphene [17, 18], $LaOBiS_2$ films [19], Bi(111) bilayer on the $MoS_2$ substrate [20], perovskite oxides [21, 22], janus transition metal dichalcogenides [23, 24], heterostructres composed of two-dimensional materials [25, 26], monolayers comprised of polar transition metal dichalcogenide [27, 28], janus (Mo/W)$GeSiP_2As_2$ monolayers [29] and recently discovered jacutingaite family [30]. Experimentally, it has been observed in BiTeI semiconductors [31], heavy metals thin film surfaces [32–35] and semiconductor quantum-wells [36, 37].

Besides the Rashba spin splitting, another type of spin splitting in non-magnetic materials is the non-magnetic Zeeman spin splitting. It has a close resemblance to the magnetic Zeeman spin splitting (see figure 1), and is very demandable in spintronics. Despite its potential application, such type of spin splitting has only been observed in the two-dimensional transition metal dichalcogenides such as $MoS_2$ and $WSe_2$ so far [38–40]. In contrast to Rashba spin splitting, the Zeeman-type splitting occurs at non-TRIMs in the Brillouin zone. Generally speaking, the absence/presence of inversion/time-reversal symmetries and the high SOC effects are recognized as the usual recipes to observe the non-magnetic Zeeman-like splitting.

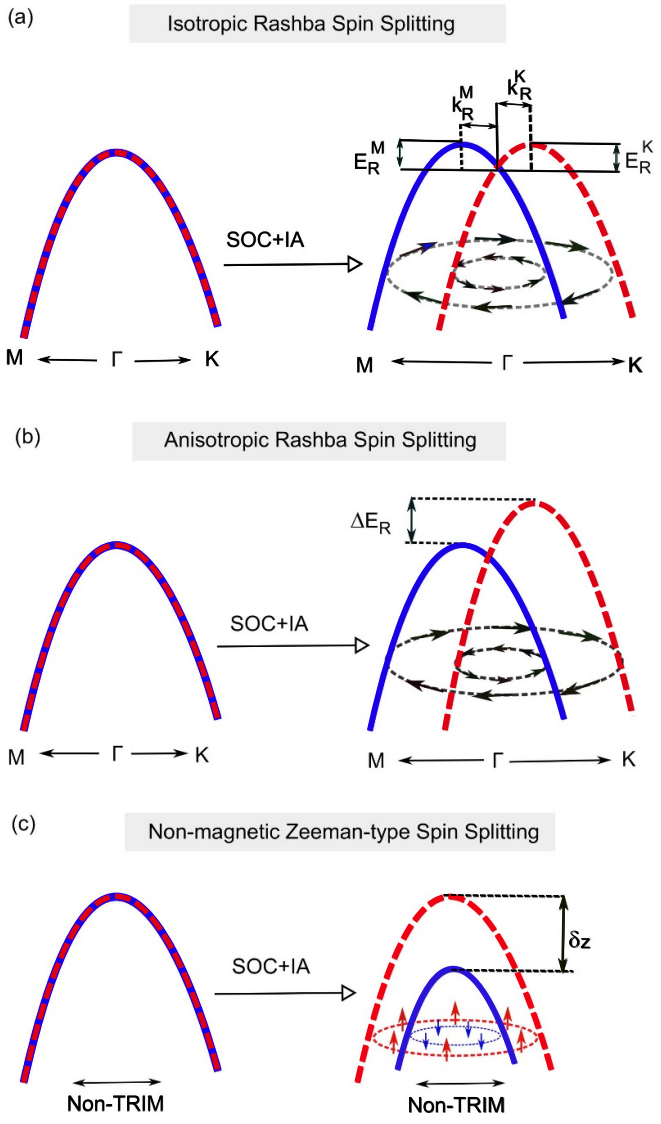


**Figure 1.** A schematic diagram describing the overall sketch of the possible spin splittings correlated with our proposed systems. (a) Isotopic Rashba spin splitting ($\Delta E_R \sim 0$): the bands (solid-blue and dashed-red) are degenerated at all $k$-points in the Brillouin zone in the absence of SOC effects. This degeneracy breaks down when SOC is switched-on except at the TRIM (say Γ-point) with spin mainly polarized in the plane of the sample. (b) Anisotropic Rashba spin splitting ($\Delta E_R \neq 0$): Similar to (a). However, for the anisotropic case, the amplitude of the spin splitting is not the same in different directions of the Brillouin zone. (c) Nonmagnetic Zeeman-type spin splitting: Bands are split at the non-TRIM without mixing the spin-up and spin-down components upon the inclusion of relativistic effects conferring a close resemblance with magnetic Zeeman spin splitting. Here IA symbolizes the inversion asymmetry.

For an influential Rashba spin splitting, the synchronous presence of two ingredients, (i) strongly broken spatial inversion symmetry and (ii) strong SOC effect, are essential. So far, for inducing or strengthening the Rashba effects in two-dimensional solids, various strategies have been adopted listed as: (i) coupled with some suitable substrate possessing strong SOC effects, (ii) decorated with heavy metallic components using the doping and adsorption approach, or (iii) applying a vertical electric field. However, from the experimental point of view, all these conventional strategies are not very straightforward to deal with in a controllable way. In this sense, systems that intrinsically possess substantial Rashba SOC are always at the first preference. Because they are usually free from the possible undesired interaction such as substrate-induced disorders/defects and doping/adsorption complications.

The materials with MX ($M$ = transition metals, $X$ = IV, V or VI elements) chemical composition exists in the bulk form with strong covalent bonding between the alternating MX monolayers. In the bulk geometry, they are topological semimetals with robust surface states. For instance, MoC, WC, TaN, and WN are triple-point topological semimetals [41, 42]. The MX family has been experimentally synthesized in the bulk form [43, 44]. However, due to strong chemical bonding between the adjacent layers, they cannot be downsized to the monolayer limit using the layer exfoliation techniques. Nevertheless, the single layer of these materials can be grown using the bottom-to-top approach as previously used for silicene and germanene synthesis [45–48].

Here in the present proposal, employing the fully relativistic calculations based on density functional theory, we proclaim largely and electrically tuaneable anisotropic Rashba-type and nonmagnetic Zeeman-type spin splitting in this transition metal based $MX$ systems. In this context, we consider $MX$ $(M = \mathrm{Mo/W}, X = \mathrm{C/S/Se})$ monolayers as an example to establish an efficient platform in the context of spin related phenomena. Our analysis should fairly applicable to other systems with same geometry, such as WN, TaN, ZrTe, MoP, MoN, NbN, NbS, etc. Indeed, this family can be an excellent platform for both the conventional and topological spintronics applications based on Rashba and non-magnetic Zeeman type spin splittings. These monolayers are crystallized in the honeycomb lattice with buckling-type structure. The existence of high anisotropic Rashba spin splitting is attributed to the broken inversion symmetry, presence of heavy components and the appearance of similar atomic and orbital characters for the electronic states around the Fermi level in these monolayers. For instance, the Rashba coefficient in the WSe is around 1.6 eV Å, which is to our knowledge larger than the similar systems reported so far. The spin splitting of the Rashba-type is usually marked around the Γ-point instead of the $M$-point due to its higher symmetric nature than the $M$-point in the Brillouin zone and this makes MX monolayers more interesting. Interestingly, the amplitude of the Rashba SOC can be further tuned with the application of external means such as symmetrical/asymmetrical strain, vertical electric field and alloy engineering. We realize the non-zero Berry curvatures arising from the opposite valleys in these MX monolayers. Due to the opposite peaks of Berry curvatures arising from the opposite valleys, these MX monolayers are intrinsic quantum valley Hall insulators. The carriers can be selectively excited from the opposite valleys using circularly polarized light as a stimulation. Furthermore, we observe that these monolayers present topological signals with robust edge states protected by time-reversal symmetry when grown in the para-electric phase. While they have Rashba-like spin-splitted edge states when grown in the ferroelectric phase.

Besides the Rashba-type spin splitting, we observe another kind of spin splitting, the so-called non-magnetic Zeeman-type spin splitting. The conduction band minima, which is located at the non-TRIM in the Brillouin zone, undergoes such kind of spin splitting (e.g. 475 meV for WSe). In order to examine the interfacial characteristics of the MX family with substrates or other solids, we also investigate the interaction of these monolayers with other two-dimensional materials following the heterostructure techniques. In this context, we deposite these MX monolayers on the $WS_2$ and GaTe substrates. In particular, WC/$WS_2$ and WC/GaTe systems display the so-called type-II band alignment, where electron and hole become layer splitting across the interface. While addressing the question, can these MX monolayers be used as external stimuli to enhance the relativistic interaction in the materials with weak SOC? We consider graphene as a prototype example where the weak SOC limits its spintronic applications. After coupling with WC monolayer, we find a large spin splitting together with a band gap at the Fermi surface of the graphene system, indicating the enhancement of SOC in the graphene system. Furthermore, depending on the stacking patterns, graphene deposited over WC monolayer passes through the phase transition from the Shotcky barrier-free contact to the semiconducting junction.

## 2. Computational approach

The first principle calculations in the framework of density functional theory were carried out using the Vienna *ab initio* simulation package [49, 50]. The interactions between the core-electrons and valence electrons were modeled in the framework of the projector augmented wave method [51]. Whereas the valence electron-electron correlation effects were modeled in the domain of generalized gradient approximation based on the Perdew–Burke–Ernzerhof (PBE) scheme [52]. The cutoff energy for the plane wave expansion was chosen to be 500 eV. The Brillouin zone was sampled using the Γ-centered k-mesh of $17 \times 17 \times 1$. All the structures were relaxed until the largest Hellmann–Feynman force on each atom is less than $-0.01$ eV Å$^{-1}$. In order to avoid the possible interactions between the periodic images, we establish a vacuum with a thickness of more than 20 Å in the normal direction of the slab. To kill out the artificial electric field caused by the periodic boundary conditions, we used the L. Bengtsson dipole correction technique [53]. We also adopted HSE06 functional in our calculations which gives a better description of the electronic excitation gap and other related properties [54]. Using the density perturbation method [55] implemented in the phonopy package [56], we carry out the dynamic

stability calculations. Relativistic effects and vertical electric field were included self-consistently. Topological properties such as Berry curvatures $\Omega_z(k)$, topological $\mathcal{Z}_2$ invariant, surface states and spin-textures are calculated using the algorithm discussed in the [57–60]. The electric field was considered self-consistently without structural relaxation.

## 3. Stable geometrical properties

Regarding the *MX* family, they are stable in the buckled trigonal structure with space group $p3m1$ (156) [41, 42, 61], as shown in figure 2. Each *M* atom is surrounded by three *X* atoms and vice versa. The relaxed structural parameters such as the lattice constants, buckling distances, band gaps, and spontaneous polarization strengths are listed in table 1. The presence of non-zero electric dipole moments in these monolayers is due to the considerable difference in the electronegativity strength of the *M* and *X* atoms and their existence in different planes (see figures 2(c) and (d)). The spontaneous in-plane polarization cancels out, whereas out-of-plane polarization exists due to the broken out-of-plane inversion symmetry. Due to the high strength of the out-of-plane spontaneous polarization and heavy components like W and Mo, the MX monolayers could be an ideal system for spin splitting with Rashba-type and non-magnetic Zeeman-like nature.

## 4. Electronic band structures

As can be displayed in figure 3, these monolayers are indirect semiconductors with valence band maximum and conduction band minimum being located at the time-reversal invariant momentum *M* and in-between the $\Gamma \rightarrow K$ line (i.e. at *Q*-point), respectively. To further analyze their band structures, we perform the orbital-projected band analysis. It reveals that the highest occupied valence and the lowest un-occupied conduction bands mainly originate from *d*-orbitals of the transition metal atoms (Mo, W), conferring a weak hybridization with the *p* states of chalcogenides (S, Se) around the Fermi level. Unlike transition metal dichalcogenides, where only the in-plane inversion symmetry $[M:(x,y)\rightarrow(-x,-y)]$ is broken while mirror symmetry ($M: z \rightarrow -z$) is preserved ($D_{3h}$ point-group), for MX monolayers, both of these symmetries are broken ($C_{3v}$ point group). This leads to a local asymmetrical potential gradient normal to the horizontal plane, which causes the Rashba spin splitting in these MX monolayers.

In the absence of SOC effects, the bands remain degenerate, as can be seen from figure 3. Observing the weighted presence of $M-d$ orbitals around the Fermi level together with broken in-plane inversion and out-of-plane mirror symmetries, we expect a large spin splitting of both Rshaba-like and Zeeman-like nature in these MX monolayers. When the SOC is switched on, band spin splitting occurs due to the inversion asymmetries in these monolayers. As can be observed from figure 4, the degeneracy at TRIM is not affected by the relativistic effect and still remains preserved due to the Kramer theorem. The conduction band minimum in these monolayers, which is located between *K* and Γ points, is firmly split. This spin splitting is further enhanced near *K*-point while decreased near Γ-point. We also observe that the valence band maximum slightly shifts from the *M*-point upon the inclusion of SOC effect, because *M*-point is time-reversal invariant and hence the spin degeneracy would be preserved at this momentum. However, the spin degeneracy is broken for momenta away from *M* toward *K*-point where the Kramer theorem is no longer held. Similarly, around the Γ-point, we also observe a strong spin splitting in the topmost valence bands. There exists anisotropic spin splitting along the $\Gamma \rightarrow M \rightarrow K$ path as displayed in figure 4. In other words, between Γ and *K* or *M* points, the Rashba spin splittings are unequal, i.e. $\Delta E_R \equiv E_R(\Gamma \rightarrow K) - E_R(\Gamma \rightarrow M) \neq 0$, where $\Delta E_R$ represents the anisotropy energy, which is a useful degree of freedom. For instance, by hole-doping, it is possible to adjust the Fermi level in one of the spin channels generating spin-polarized currents. The spin splitting around the *M* and Γ points reveals a close resemblance to the Rashba spin splitting of the semiconductor quantum-wells or surfaces of heavy metals.

## 5. Nature of observed spin splitting

To examine the nature of spin splitting, either its Zeeman-like or Rashba-like, we perform the spin-projected band structure calculations. The spin projected band structures are displayed in figure 5. First, we focus on the top valence bands. As can be seen, around the Γ-point, the spin components $\sigma_x$ and $\sigma_y$ are dominated. It indicates that the spin is distributed in the plane of these monolayers with a vanishing contribution from the out-of-plane spin projection component $\sigma_z$, confirming a Rashba-like nature, where the spin distributes in the plane of the sample. Slightly away from the Γ-point toward the *K*-point, the spin tends to align in the vertical direction, showing the decreasing of Rashba-like character. The conduction band minimum is dominated by the $\sigma_z$ component, which is a clear indication of the nonmagnetic Zeeman-like spin splitting (see figure 5). We also analyze the two-dimensional spin pattern in the vicinity of the Γ-point in the two-dimensional $(k_x - k_y)$ plane, which is displayed in figures 6(a)–(c), reflecting a Rashba-type behavior.

To competently understand the spin splitting, we show the $k_{\|}$ dependence of the spin splitting $\Delta E_{12}$ for the top valence bands $V_{tvb}$ and $V_{tvb}-1$ in figure 5(d). As can be perceived, both bands display a complex behavior in terms of spin splitting. In the vicinity of Γ-point, the peaks in the spin splitting $\Delta E_{12}$ are not at the same level along the $\Gamma \rightarrow K$ and $\Gamma \rightarrow M$ directions, signifying a high anisotropic spin splitting mode.

A two-dimensional system with $C_{3v}$ symmetry can be described by the following effective Hamiltonian [31, 62],

$$H = \alpha_R(k_x\sigma_y - k_y\sigma_x) + \lambda k^3 cos(3\theta)\sigma_z. \quad (1)$$

This expression has two contributions, i.e. one is the first-order linear term while the other is a third-order term. Here, $\alpha_R$ and $\lambda$ describe the Rashba coefficient and warping parameter, respectively. As can be noticed from the above expression, first and second terms correspond respectively to the in-plane and out-of-plane spin polarizations, where $\theta = \cos^{-1}[k_x/k]$. Note

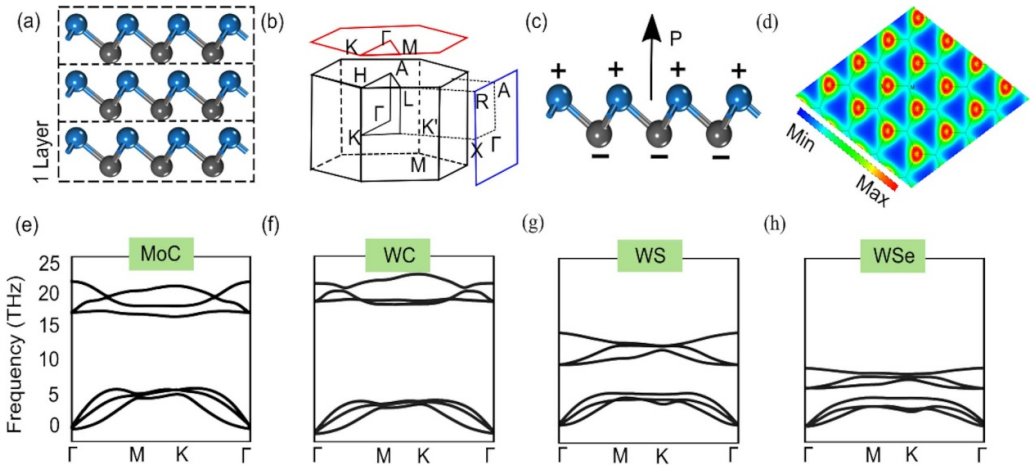


**Figure 2.** (a) Crystal structure of MX solids in the bulk geometry. (b) Three-dimensional first Brillouin zone in the $k$-space. (c) MX monolayers in the two-dimensional geometry. (d) Planer electronic charge density for *WC* system in the (001) plane. Phonon dispersion spectrum for the MoC (a), WC (b), WS (c), and WSe (d) in the single-layer form. The nonexistence of imaginary modes in the spectrum is an indication of the dynamic stability of these MX monolayers.

**Table 1.** Relaxed structural geometry including equilibrium lattice parameters ($a = b$), buckling height ($h_z$) parameterized by the distance between the $M$ and $X$ atoms, and spontaneous polarization ($P$) measured with PBE functional. Electrical transport energy gaps parameterized by the global ($Eg$) and direct ($E_{dg}$) bandgaps calculated with HSE06 + SOC functional.

| Parameters | MoC | WC | WS | WSe |
|---|---|---|---|---|
| $a$ (Å) | 3.01 | 3.01 | 2.96 | 3.02 |
| $h_z$ (Å) | 0.9 | 0.94 | 1.62 | 1.74 |
| $P$ (pCm$^{-1}$) | 14.96 | 11.68 | 3.06 | 4.52 |
| | | HSE + SOC | | |
| $E_g$ (eV) | 1.26 | 1.57 | 0.56 | 0.42 |
| $E_{dg}$ (eV) | 1.68 | 1.62 | 0.98 | 0.66 |

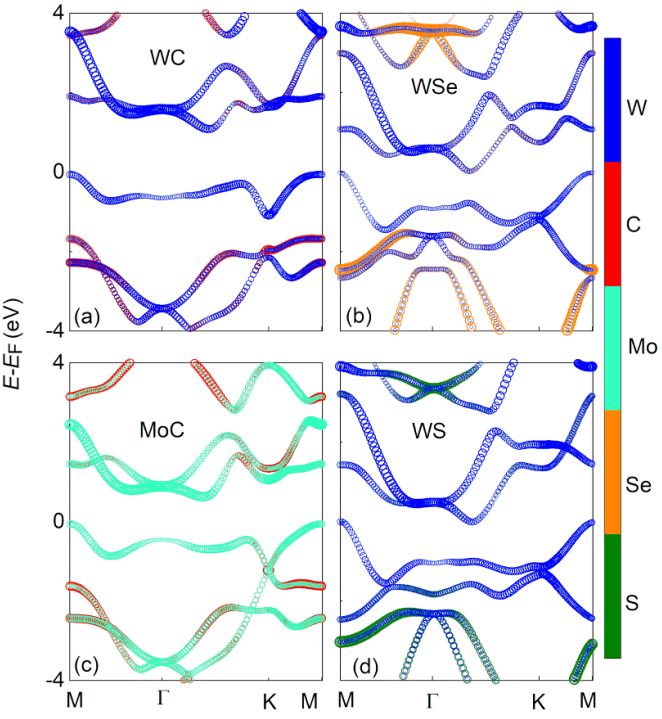


**Figure 3.** The atomic resolved band structures of *MX* monolayers without considering the relativistic effects for WC (a), WSe (b), MoC (c), and WS (d) calculated with the PBE functional. The dominant $M - d$ and $X - p$ orbital contributions are given in color. In all these systems, the valence band maximum is located at the time-reversal invariant momentum $M$, whereas the conduction band minimum is located in-between the Γ and $K$ points (i.e. at $Q$-point). The bands around the Fermi level mainly originate from $M$ atoms.

that the $k_x$ axis is chosen to be along the $\Gamma \rightarrow K$ direction, means $\theta = 0$ along $\Gamma \rightarrow K$ direction, while $\theta = \pi/2$ for $\Gamma \rightarrow M$ direction. From the spin projection plots (figure 5), it is clear that there is no out-of-plane spin polarization along $\Gamma \rightarrow M$ direction, which is consistent with our effective Hamiltonian defined in equation (1) for $\theta = 0$. Similarly, in the vicinity of Γ-point along the $\Gamma \rightarrow K$ direction, the dominant spin components are $\sigma_x$ and $\sigma_y$, showing in-plane spin polarization. However, slightly far away from Γ-point along the $\Gamma \rightarrow K$ direction, the spin tends to polarize in the out-of-plane direction and the trigonal corrections are not negligible in that region. This is also consistent with the Hamiltonian (1) for $\theta = \pi/2$. Furthermore, we also examine the spin distribution around the $M$-point and find that the spin is mainly distributed within the plane, indicating a Rashba-type behavior.

Under the first-order approximation, two parameters typically determine the Rashba SOC in a material, the momentum offset $k_R$ and energy difference $E_R$. These two quantities are related through the Rashba coefficient $\alpha_R = 2E_R/k_R$. Hence, solids with smaller (larger) $k_R$ has a larger (smaller) Rashba coefficient $\alpha_R$. However, on the other hand, the materials with large $k_R$ are also exciting and useful in the sense of sustaining the Rashba spin splitting up to very large momentum in the Brillouin zone. We notice that the MX family sustains the Rashba spin splitting up to very large momentum (see table 2) and seems very useful to sustain the spin splitting up to the large area of the Brillouin zone. We only consider the first-order contribution to the Hamiltonian to

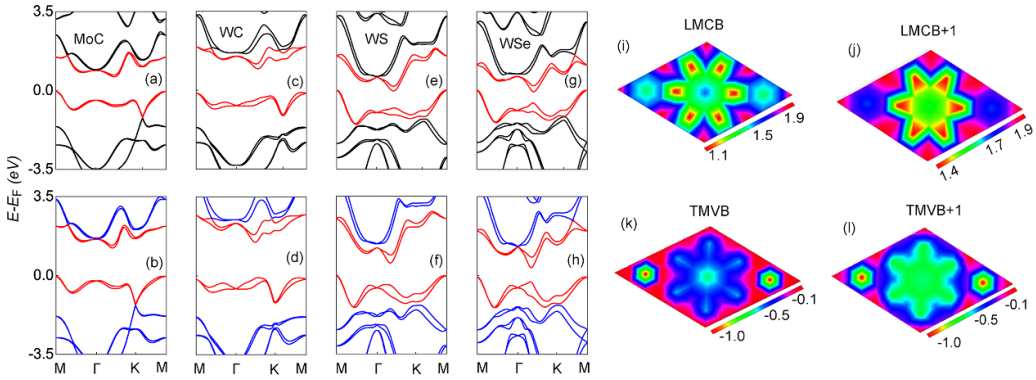


**Figure 4.** The band structures of MX monolayers by including relativistic effects for MoC (a), (b), WC (c), (d), WS (e), (f), and WSe (g), (h) monolayers. The upper ((a), (c), (e) and (g)) and lower ((b), (d), (f) and (h)) panels are calculated with the PBE + SOC and HSE06 + SOC functionals, respectively. For clear demonstration, the top valence and conduction bands are highlighted with red colors. Distribution of the lowermost conduction bands ((i), (j)) and topmost valence bands ((k), (l)) over the two-dimensional momentum space. LMCB and TMVB represent the lowermost conduction and the topmost valence bands, respectively.

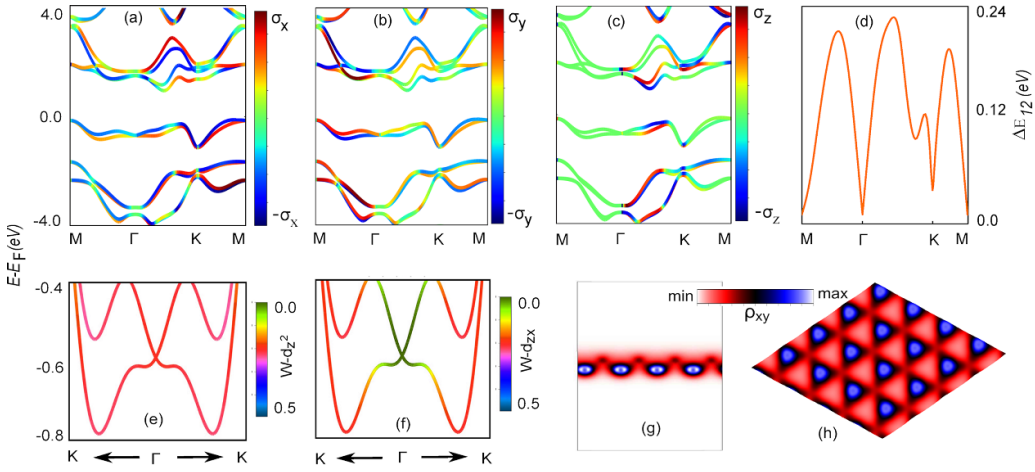


**Figure 5.** Spin-resolved band structures for the WC system with SOC effects are included. Band structures for $\pm\sigma_x$ (a), $\pm\sigma_y$ (b), and $\pm\sigma_z$ (c) spin components. (d) Variation of the spin splitting size between the top valence bands (labeled as $V_{tvb}$ and $V_{tvb}-1$ in the text) against the in-plane momentum $k_{\|}$, calculated with PBE + SOC functional. (e) and (f) The orbital resolved bandstructre in the vacinty of Γ-point, the contribution of W-$d_{z^2}$ (e) and W-$d_{zx}$ (f) are shown. (g) and (h) The in-plane charge density variation in top (g) and side view appearance (h).

extract Rashba parameter $\alpha_R$. We observe that the spin splitting in the MX monolayers exhibits different amplitudes along different paths in the Brillouin zone, indicating high anisotropic behavior. In particular, around the Γ-point, the amplitude of Rashba spin splitting is not equal to that along $\Gamma \rightarrow K$ and $\Gamma \rightarrow M$ directions. Consequently, the splitting amplitudes are also highly anisotropic around $M$-point for $M \rightarrow K$ and $M \rightarrow \Gamma$ directions. The amplitudes of Rashba spin splitting $E_R$, Rashba coefficient $\alpha_R$ and momentum offset $k_R$ along different directions in the Brillouin zone are listed in table 2. As can be noticed from table 2, our proposed systems display higher Rashba spin splitting in comparison to the previous systems, including typical semiconductors based heterostrucutres ($In_{0.05}Ga_{0.95}As/GaAs$ ($\alpha_R \sim 80-120$ meV Å) [63], $In_{0.53}Ga_{0.47}As/In_{0.52}Al_{0.48}As$ ($\alpha_R \sim 70$ meV Å) [64], $GaSe/MoSe_2$ ($\alpha_R \sim 490$ meV Å) [26]), and thin films composed of heavy elements such as Au(111) surfaces ($\alpha_R \sim 330$ meV Å) [65] and Bi(111) surfaces ($\alpha_R \sim 550$ meV Å) [66].

We notice that the Rashba parameter $\alpha_R$ is larger in $WX = (X = C, S, Se)$ than that in $MoX = (X = C, S, Se)$ due to the larger SOC effects in $W$. Furthermore, we observe a high amplitude of spin splitting in the conduction band minimum with a non-magnetic Zeeman-type nature, which is located in-between the Γ and $K$ high symmetric line. The size of the Zeeman spin splitting at the conduction band minimum is observed to be within 117–475 meV for MX systems, which is notably high as compared to the two-dimensional transition metal dichalcogenides ($WSe_2$, $WS_2$, and $MoSe_2$) with conduction band minimum spin splitting predicted to be in the 1–40 meV range.

The epitaxial growth of two-dimensional materials, especially the one-layer thick solids require a proper substrate. And thus the substrate can affect the intrinsic properties of these freestanding MX monolayers and its role cannot be ignored in the spin splitting context as well [67, 68]. Indeed the substrate, both in a positive and negative sense, can affect the size of spin splitting in these freestanding MX monolayers [67, 68]. In

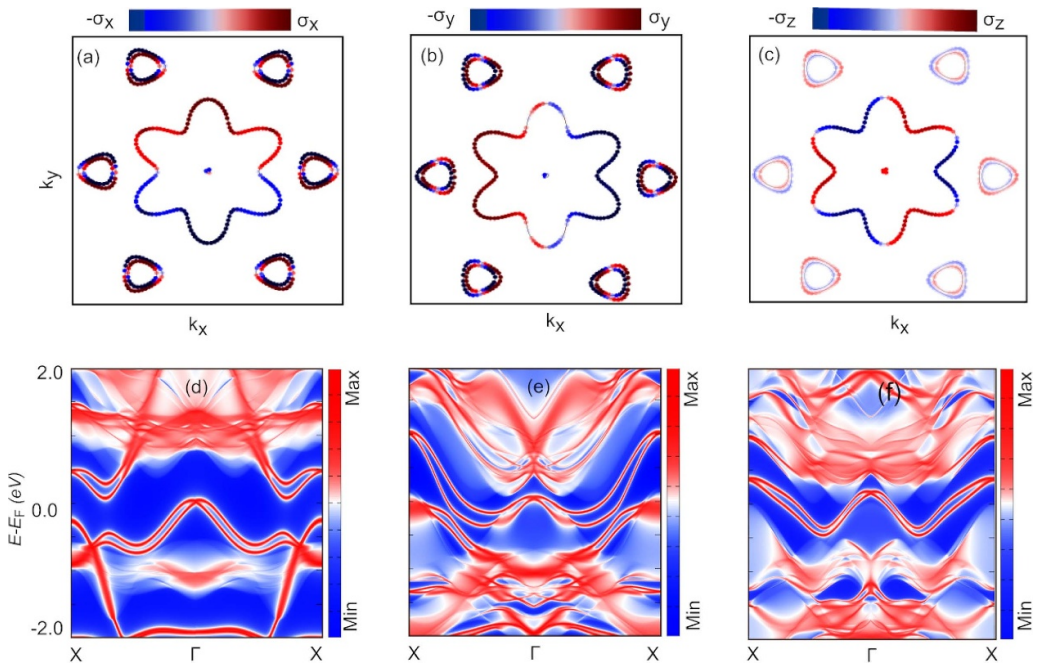


**Figure 6.** Spin texture distribution maps in the plane of WC monolayer at the constant energy cut E = $E_F$-0.609 eV for $\pm\sigma_x$ (a), $\pm\sigma_y$ (b), and $\pm\sigma_z$ (c) spin components. (d), (e) Surface states of WC (d), WS (e), and WSe (f) monolayers.

**Table 2.** Listed amplitudes of the Rashba spin splitting $E_R$, corresponding momentum offsets $k_R$, and Rashba coefficients $\alpha_R$ in top valence bands along different directions in the first Brillouin zone together with the amplitudes of nonmagnetic Zeeman-type spin splittings $\delta_z$ in the lower conduction band for the proposed MX monolayers. Here, the $\delta_z^{\mathrm{CBM}}$ symbolizes the Zeeman-type splitting in the conduction band minimum (CBM) located in-between the $\Gamma \rightarrow K$ path, whereas $\delta_z^{\mathrm{K}}$ describes the Zeeman-type spin splitting in the lower conduction band at the $K$ valley point. Numerals outside (inside) the round-brackets correspond to the PBE + SOC (HSE06 + SOC) functionals.

| | Rashba Spliting | | | | | | | | | Zeeman spin splitting | |
|---|---|---|---|---|---|---|---|---|---|---|---|
| | $\Gamma \rightarrow K$ | | | $\Gamma \rightarrow M$ | | | $M \rightarrow K$ | | | $\Gamma \rightarrow K$ | $K$ |
| System | $E_R$ (meV) | $k_R$ (Å$^{-1}$) | $\alpha_R$ (meV Å) | $E_R$ (meV) | $k_R$ (Å$^{-1}$) | $\alpha_R$ (meV Å) | $E_R$ (meV) | $k_R$ (Å$^{-1}$) | $\alpha_R$ (meV Å) | $\delta_z^{\mathrm{CBM}}$ (meV) | $\delta_z^{\mathrm{K}}$ (meV) |
| MoC | 4.12 | 0.056 | 147 | 4 | 0.049 | 163 | 1.6 | 0.023 | 139 | 73 | 30 |
| | (11.25) | (0.09) | (281) | (11.22) | (0.09) | (249) | (4) | (0.05) | (160) | (117) | (44) |
| WC | 159 | 0.31 | 1025 | 155 | 0.33 | 939 | 32.32 | 0.147 | 439 | 216 | 274 |
| | (287) | (0.37) | (1551) | (240) | (0.37) | (1297) | (55) | (0.18) | (611) | (331) | (360) |
| WS | 114 | 0.19 | 1200 | 94 | 0.19 | 989 | 2.5 | 0.02 | 250 | 207 | 170 |
| | (139) | (0.25) | (1112) | (117) | (0.25) | (936) | (4.32) | (0.06) | (144) | (356) | (260) |
| WSe | 120 | 0.19 | 1263 | 97 | 0.17 | 1141 | 3.8 | 0.03 | 281 | 271 | 94 |
| | (153) | (0.19) | (1610) | (100) | (0.19) | (1053) | (9) | (0.06) | (300) | (475) | (137) |

the presence of substrate, these freestanding MX monolayers can form new chemical or Van der Waal bonds at the interface depending on the composition of chosen substrate and its chemical reactivity. In principle, different parity orbitals can establish an interatomic coupling at the interface, resulting in $k$-dependent orbital angular momentum [68]. It can quench or enhance the size of giant spin splitting in these freestanding MX monolayers. However, how specifically substrate affects the spin splitting in our proposed freestanding MX monolayers is outside the scope of this study.

Recently, the role of unquenched orbital angular moment in the giant spin splitting was realized [69–72]. It was shown that the competition among three major terms, namely crystal-field (depends on the crystal symmetry), atomic SOC (depends on the atomic number Z), and electrostatic energy (stems from the coupling of asymmetric charge distribution and surface electric field), define the accurate energy scale of the observed spin splitting in a system [72]. In the weak (strong) SOC regime, the atomic SOC (electrostatic energy) is the relevant energy splitting scale of the system. This orbital angular momentum based mechanism successfully predict the energy scale for Rashba-type band splitting in several systems such as: Au(111) [67, 72], $Bi_2Te_2Se$ [72], and $WSe_2$ [67]. Thus it is important to shed light on the scale of the observed energy splitting in our proposed MX monolayers. In this context, by examining the top valence band around the Γ point in the WC monolayer, we realized that the main contribution is coming from the W-$d_{z^2}$ orbital, which consequently couple with the $d_{zx}$

($d_{zy}$) orbital along the $k_x$ ($k_y$) direction (see figures 5(e) and (f)), producing nonzero $\langle L_x \rangle$ or $\langle L_y \rangle$ components. Therefore, we expect the unquenched orbital angular momentum in our MX monolayers. This unquenched orbital angular momentum couple with crystal momentum and as a result asymmetric charge distribution is formed which can be seen in the Charge density of WC monolayers (see figures 5(g) and (h)).

On the basis of above, we believe that broken mirror symmetry in our proposed MX monolayers establish an interatomic hopping between different-parity orbitals, which generates wavefunctions with nonzero orbital angular momentum near heavy element nucleus. This orbital angular momentum, couples with the spin via strong atomic SOC of heavy atoms, such as W and Mo, resulting in giant spin-splitting. We realize that the W based MX monolayers whose atomic SOC is stronger than that of Mo based monolayers (see table 2 and figure 4) shows a larger Rashba splitting in its band structure. This indicates that the scale of the Rashba splitting is clearly linked to the atomic SOC strength in our proposed monolayers. And hence, the observed spin splitting in our proposed monolayer is expected to govern by the atomic SOC [67, 68, 72].

## 6. Topological analysis and valley contrasting Berry curvatures

To assess the topological signature of the MX family, we perceive the surface states of WC, WS and WSe monolayers. As can be seen from figures 6(d)–(f), these monolayers exhibit surface states that cross each other at the TRIM (i.e. at Γ-point). By closely examining the surface states, it can be seen that they are not like topological insulators because they are not connecting the $V_{tvb}$ and $C_{lcb}$ bulk bands through the bulk energy gap. However, they have a close resemblance with bands splitted via Rashba SOC. Thus, we can call the WC family an ordinary band insulators with Rashba-like spin splitted edge states.

Interestingly, by closely observing the band structures of MX monolayers, especially the lower conduction band, the valleys can be seen around the Q/Q' points in the Brillouin zone (see figures 7(a)–(d) and 8(c), (d)). We label these valleys by Q and Q', in a similar way as we label K and K' valleys in transition metal dichalcogenides. From these valleys, opposite peaks of the Berry curvature arise (see figures 7(a)–(d)) (i.e. valley contrasting Berry curvatures). Due to the valley contrasting Berry curvature together with the large global band gap, these MX monolayers are intrinsic quantum valley Hall insulators. We also calculate the circular dichroism distribution by shining the left and right handed circularly polarized light upon these MX monolayers. From the circular dichroism pattern in the momentum space (see figures 7(e)–(h)), it is clear that carriers belonging to opposite valleys are selectively excited depending on the polarity of the shining circularly polarized light. Thus, these MX monolayers are useful for the spin valley and valley-contrasting Berry curvature applications.

In below, we shed light on the possible functionalization of the Rashba-like and Zeeman-like spin splitting in these monolayers. The amplitude of the spin splitting can be tuned with the application of external operations such as strain, vertical electric field or alloy engineering.

## 7. MX monolayers in paraelectric phase

The electronic properties of these MX monolayers in the paraelectric phase are presented in figure 9. As can be noticed, these MX monolayers exhibit unusual band structures in the vicinity of the Fermi level around the Γ point. In the paraelectric phase, these MX monolayers possess massless quadratic Dirac type spectra that are shown in figures 9(a), (c), (e) and (g). The states around these massless Dirac cones originate from the $|l = 2, m_l = \pm 1\rangle$ orbitals (i.e. $d_{yz}$ and $d_{xz}$), which can be seen from the orbital projected band structures as shown in figures 9(a), (c), (e) and (g). In the case of WS and WSe, these band-touching responses locate around the Fermi surface, while above the Fermi surface for the cases of WC and MoC systems. Observing the inversion of the band order around the Γ point in these MX monolayers, which is considered as a primary signature for the topological behavior in solids, these band-touching responses may lead to topological hallmarks. After introducing the relativistic interaction, the states $d_{yz}$ and $d_{xz}$ tend to repel each other and a non-zero band gap appears around the Γ point, which converts these massless Dirac cones into a massive one (see figures 9(b), (d), (f) and (h)). The local direct band gaps at Γ point triggered by SOC are estimated to be 95, 307, 208 and 176 meV for MoC, WC, WS, and WSe, respectively. We further confirm the topological responses in these MX monolayers by calculating the surface states using the tight-binding approach as implemented in Wannier90 and Wanniertools packages [57–59]. As can be observed from figures 9(i)–(l), the Kramer partners combine at the TRIM point (Γ) and make a massless surface Dirac cone, which provides the topological protection against non-magnetic perturbations. However, due to the negative global band gap, these MX monolayers can not be accepted as $Z_2$ topological insulators. Alternatively, these MX monolayers can be called $Z_2$ topological semi-metals or metals due to having a non-zero local bulk band gap extended throughout the Brillouin zone and robust gapless edge states [73].

In the MX monolayers, polarization can be switched from $-P$ to $+P$ by folding the direction of the $M - X$ bonds. Alternatively, the transformation between the $+P$ and $-P$ polarization states can be controlled by changing the buckling distance from $h_z > 0$ to $h_z < 0$ in these MX monolayers. The size of the polarization switching barrier is an important parameter in ferroelectrics and needs to be evaluated. We define the polarization switching barrier energy as $E_b = E(h_z) - E(h_0)$, where $E(h_z)$ and $E(h_0)$ are the energies at different buckling heights and equilibrium buckling heights, respectively. In order to evaluate the switching energy barrier $E_b$ in the WC monolayer, we performed a series of calculations. The switching energy

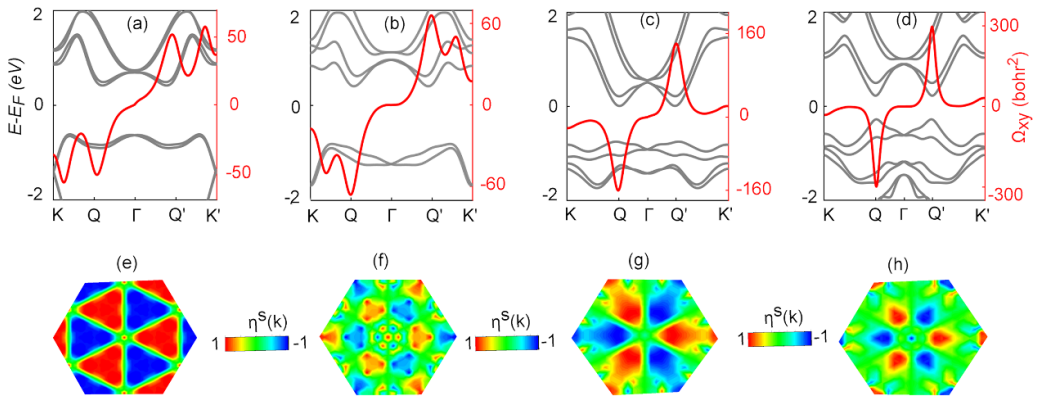


**Figure 7.** Berry curvature distributions along the high symmetry $k$-points for the MoC (a) WC (b), WS (c) and WSe (d) monolayers. The valley contrasting behavior of the Berry curvature around the valley points $Q$ and $Q'$ can be noticed. The valley-driven circular dichroism distribution maps for the right-handed circularly polarized light for MoC (e), WC (f), WS (g), and WSe (h) monolayers.

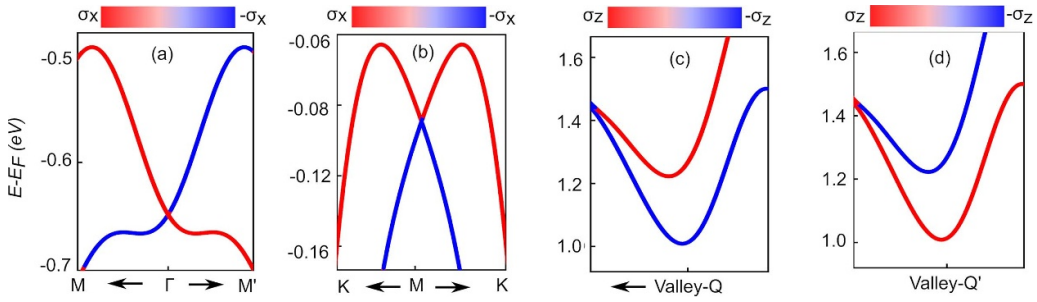


**Figure 8.** Spin resolved band structures of WC monolayer. (a) and (b) Topmost two valance bands projected on the $\pm\sigma_x$ spin component in the vicinity of Γ-point (a) and $M$-point (b). (c) and (d) Lowermost two conduction bands projected on the $\pm\sigma_z$ spin component in the vicinity of $Q$ (c) and $Q'$ (d) valleys.

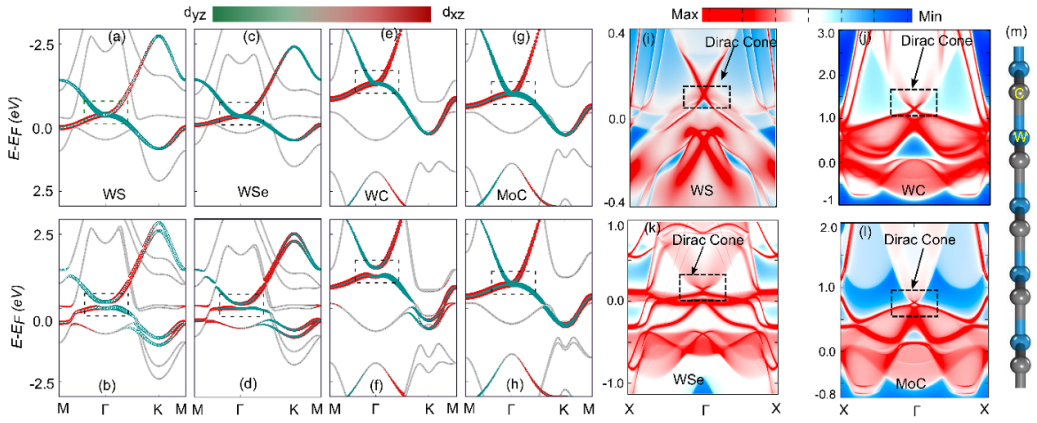


**Figure 9.** Band structures of MX monolayers in paraelectric phase with net polarization $P_z = 0$. The upper (lower) panel corresponds to the band structures in the absence (presence) of SOC effects. The appearance of quadratic type Dirac behavior in these monolayers are enclosed in dashed-line boxes. The surface states of WS (i), WC (j), WSe (k) and MoC (l); Dirac cones are visible near the Fermi surface (see the regions enclosed by dashed-line boxes) ensuring the topological protection in the MX family when grown in the form of para-electric geometry. (m) The lattice structure of the paraelectric WC layer.

barrier $E_b$ for the WC monolayer is estimated to be ∼0.9 eV. However, this energy barrier is very high and require a strong electric field outside the experimentally accessible range. We also calculated the energy barrier for WS and WSe monolayers which are even much higher [2.56 eV for WS and 2.70 eV for WSe]. All these results demonstrate that the WC monolayer has spontaneous polarization, however, it is very hard to be switched.

## 8. Symmetrical strain effects

Strain engineering is always recognized as superior for tuning electronic properties due to its clean nature in contrast to chemical doping and adsorption. Figure 10 presents the variation of band structures against the symmetrical strain, defined as $\eta_{xx} = \eta_{yy} = (a_{\text{sub}} - a_{\text{MX}})/a_{\text{MX}}$ with $a_{\text{sub}}$ and $a_{\text{MX}}$ representing the lattice parameters of the chosen substrate and MX

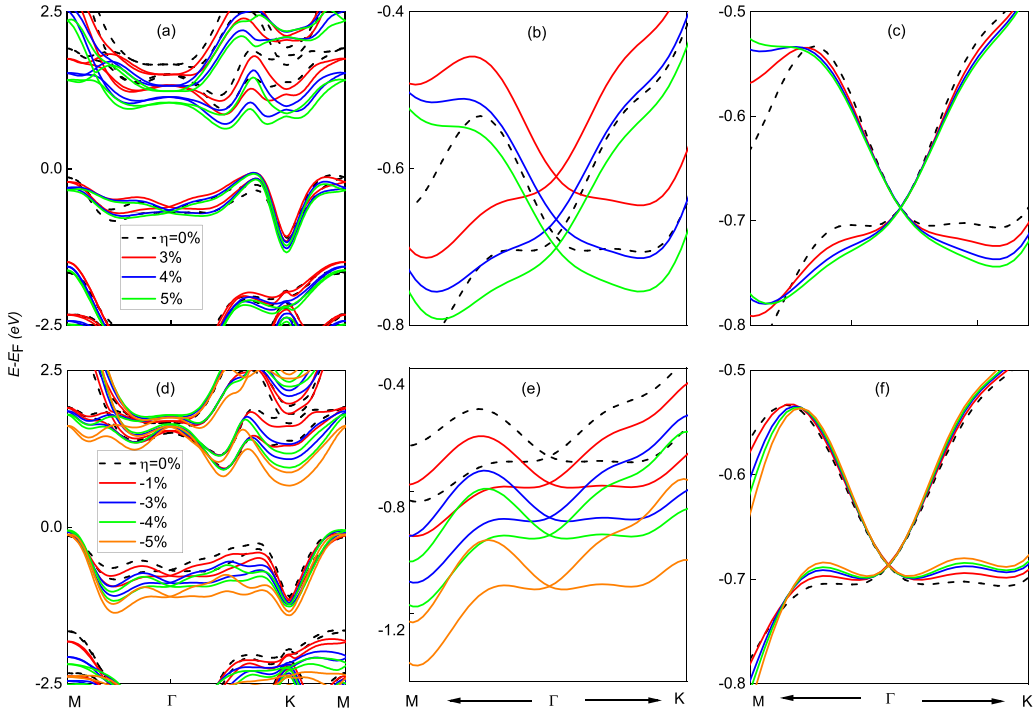


**Figure 10.** Modification in the band structure by subjecting WC monolayer to various amounts of symmetrical strain (i.e. $\eta_{xx} = \eta_{yy}$) calculated with the PBE + SOC functional. The upper/lower panel corresponds to the stretching/compression of the WC lattice. (a) Total electronic band structure of strained WC for various amounts of biaxial tensile strain. (b) Magnified view of the band structure of top valence bands around the Γ-point in (a). (c) For a clear illustration of the spin splitting variation against biaxial strain, we adjusted the crossing points at the Γ-point in (b) by adding or subtracting a constant energy shift. The lower panels (d)–(f) correspond to the compression of the WC lattice with each sector having the same description as the upper panel (a)–(c).

monolayer, respectively. Such type of strain can be practically applied by epitaxially growing these monolayers on the substrate with a larger/smaller lattice parameter. Overall, according to our calculations, strain affects the band structures of the MX monolayers by shifting their band edges, curvatures and the effective mass of carriers together with the amplitudes of the Rashba and Zeeman type spin splittings, which can be observed from figure 10. For better visualization of the spin splitting with strain, we adjusted the crossing points at the Γ point by adding or subtracting a constant energy (see figures 10(c) and (f)).

For instance, along the $\Gamma \rightarrow M$ direction, the Rashba spin splitting enhances/suppresses by compressing/stretching the WC system. This conclusion is consistent with previous work for other systems [23]. The use of symmetrical strain also enhances the magnitude of anisotropy $\Delta E_R$ in the Rashba spin splitting between the $\Gamma \rightarrow K$ and $\Gamma \rightarrow M$ directions. Around $-5\%$ strain, the conduction band minima shifts to the $K$ point with large non-magnetic Zeeman-type spin splitting (see figure 10(d)). Additionally, the position of the crossing point around the Γ point can be tuned in the vertical direction by applying the strain (see figures 10(b) and (e)).

As mentioned, strain can be applied to these freestanding MX monolayers by growing over the substrate with lattice mismatch (i.e. making mismatched vertical heterostructures). Therefore, our findings, which are mainly based on the consideration of isolated freestanding monolayers can alter due to the asymmetrical environment and chemical reactivity of the chosen substrate. Our observed features for freestanding MX monolayers can in-principle be enhanced or even quenched, depending on the interlayer coupling strength and parity of the resultant orbitals [74].

## 9. Lattice distortion

In principle, the spin splitting can be made more pronounced; even the bands without spin splitting can be split by lowering the $C_{3v}$ symmetry to $C_3$ (i.e. breaking $\sigma_v$). This can be done by applying a small Zeeman field parallel to the $C_3$ axis or by a lattice distortion using the uniaxial strain. In this context, we implement the uniaxial strain $\eta_{xx}$ along the zigzag direction. We observe that this asymmetrical strain is more efficient in the sense of tuning the amplitude of Rashba-type spin splitting, indicating a strong link between the lattice distortion and strength of Rashba SOC (see figure 11). This appends one factor more, the so-called lattice distortion, in the typical existing perceptions that Rashba spin splitting is only sensible to the SOC and electric-field effects.

In MX monolayers, the three-folded rotational $c$ axis lies in three equivalent mirror planes containing the lines joining the two time-reversal invariant high-symmetry $M$ points. Enforcing the uniaxial strain along the armchair or zigzag direction can lower this reflection symmetry, and as a result the observed spin splitting becomes more pronounced and visible. Overall, as can be seen from figures 11(b) and (f), the Rashba spin splitting in the top valance band decreases/increases by

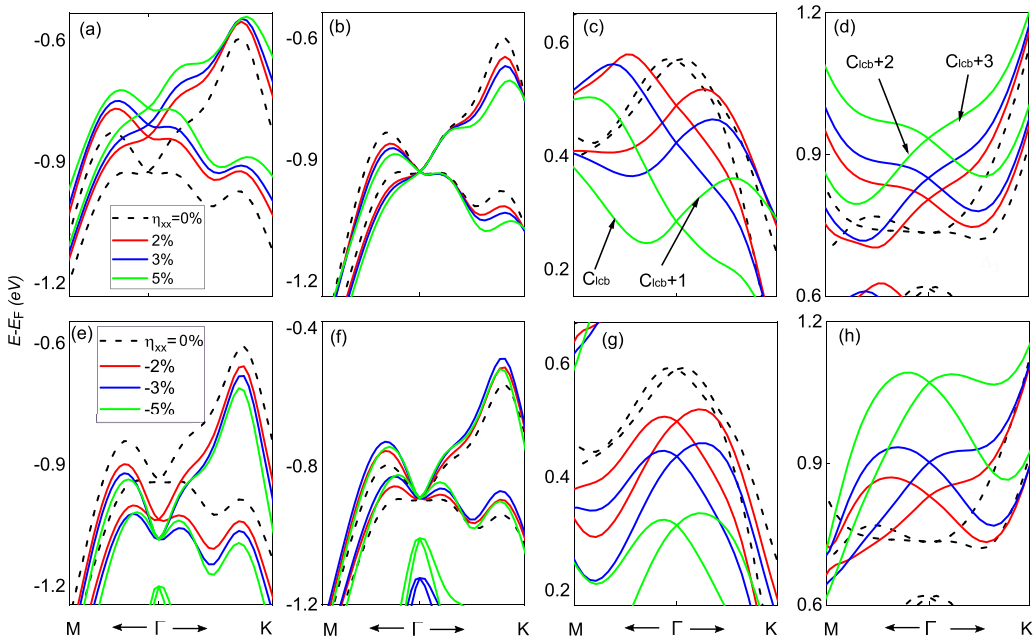


**Figure 11.** Modification in the band structure by subjecting WSe monolayer to various amounts of asymmetrical strain (i.e. $\eta_{xx}$ only) along the zig-zag direction calculated with the PBE + SOC functional. The upper/lower panel corresponds to the stretching/compression of the WSe lattice. (a) Magnified view of the band structure of top valence bands around the Γ-point. (b) For a clear illustration of the spin splitting variation against asymmetrical strain, we adjusted the crossing points at the Γ-point in (b) by adding or subtracting a constant energy shift. (c) Zoom view of the band structure of lower conduction bands, labeled as $C_{lcb}$ and $C_{lcb}+1$ inside the plot, in the vicinity of Γ-point. (d) Zoom view of the band structure of lower conductions bands labeled as $C_{lcb}+2$ and $C_{lcb}+3$ inside the plot, around the Γ-point. The lower panel ((e)–(h)) corresponds to the compression of the WSe lattice along the zigzag direction with each sector having the same description as the upper panel.

allowing the stretching/compression of the MX monolayers along the zigzag direction. For instance, for the WSe monolayer, the Rashba spin splitting $E_R$ in the top valence band increase to 374 meV along the $\Gamma \rightarrow K$ direction for the $-5\%$ uniaxial strain. Interestingly, with lattice distortion, in addition to the enhancement of Rashba coefficients in the valence band, new band spin splitting in the the lower conduction bands also appears (see figures 11(c), (d), (g) and (h)). In particular, the lower conduction bands, denoted as $C_{lcb}$ and $C_{lcb}+1$ in figure 11, split around the Γ point where the spin splitting was zero before distortion. Similarly, a large spin splitting can also be observed between the conduction band $C_{lcb}+2$ and $C_{lcb}+3$ upon the uniaxial strain, where $C_{lcb}$ denotes the lowest conduction band (see figures 11(d) and (h)). Thus, imposing the asymmetrical strain along different directions (armchair or zigzag), the Rashba interaction can be strengthened more effectively in these MX monolayers. The asymmetrical strain, in contrast to symmetrical strain, introduces more anisotropy in the spin splitting along different directions as can be perceived from figures 10 and 11. Thus, asymmetrical strain strongly enhances the anisotropic degree $\Delta E_R$ in the MX monolayers.

## 10. Application of electric field

Previous studies show that the electric field can be used as an effective external tool to tune the amplitude of Rashba-type spin splitting. Following a similar route, we expose these MX monolayers to the vertical electric-field ranging from $-0.50$ to 0.50 V Å$^{-1}$. Figure 12 exhibits the evolution of the band structure of the WC monolayer with the applications of the vertical electric field. The use of the electric field in the direction parallel/anti-parallel to the spontaneous polarization should intensify/weak the strength of Rashba spin splitting. Indeed it is the case, as can be verified from figure 12. Typically, the parallel/antiparallel setup of the electric field will raise/drop the magnitude of the internal electric field, which influences the spin splitting in the material. For example, the magnitude of the Rashba spin splitting $E_R(\Gamma \rightarrow K)$ for WSe grows to 135, 164 and 176 meV at the electric-fields with magnitudes 0.2, 0.4 and 0.5 V Å$^{-1}$ respectively.

The anisotropic energy spin splitting $\Delta E_R$ in the top valence bands is also enhanced with the application of the vertical electric field. From figure 12, it can be perceived that the size of the $\Delta E_R$ enlarges by increasing the strength of the electric field in the vertical direction. Thus, by suitably combing with an electron/hole doping strategy, this anisotropic energy spin splitting $\Delta E_R$ can be used as an effective degree of freedom to equip the desired spin channels at the Fermi surface.

## 11. Charge doping and spintronics device formation

The charge doping or electrostatic doping is now acknowledged as one of the practical tools to control the electronic

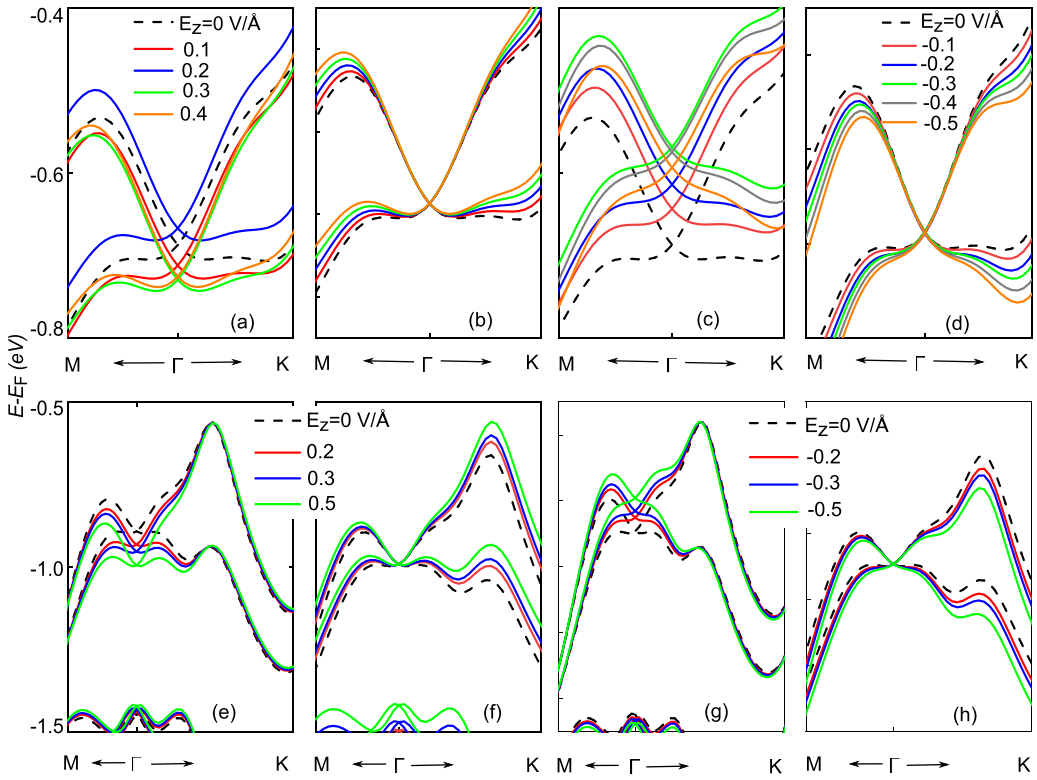


**Figure 12.** Modification in the dispersion of the top valence bands around the Γ-point by subjecting WC and WSe monolayers to various strengths of the electric field (strengths of electric field are mentioned inside the plots) calculated with the PBE + SOC functional. The upper ((a)–(d)) and lower ((e)–(h)) panels correspond to the WC and WSe system respectively. (a) Magnified view of the band structure of top valence bands around the Γ-point. (b) For more clear visualization of the spin splitting variation against an electric field, we adjusted the crossing points at the Γ-point in (a) by adding or subtracting a constant shift in energy scale. Similarly, (c) and (d) are for the negative electric field. The lower panel ((f), (g), (h) and (i)) is for the WSe system with each sector has the same description as of the upper panel.

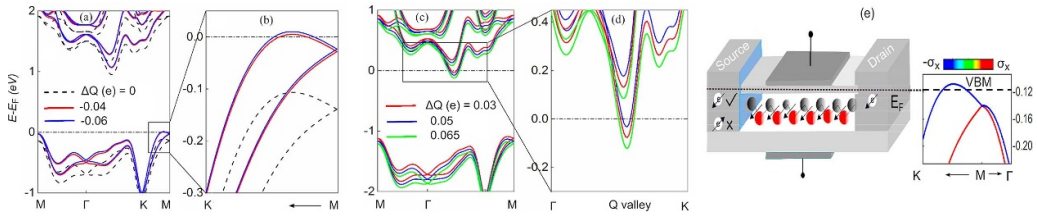


**Figure 13.** The modification in the electronic band structure by subjecting WC monolayer to various amounts of electron/hole doping controlled via electrostatic doping techniques. The Fermi level is set to zero and shown by the dotted horizontal line. (a) The band structure of the hole-doped WC monolayer for various magnitudes of hole-doping (shown inside the plot). (b) Zoom view of the band structure shown in (a) in the vicinity of the valence band maximum. (c) Band structure of the electron-doped WC monolayer for different magnitudes of the doped charge (which are shown inside figure). (d) Zoom view of the band structure in the vicinity of conduction band minimum. (e) Schematic representation of the spin filter device for the WC system lightly doped with hole. Only the in-plane spin component crosses the Fermi level and hence supporting the spin-polarized transport at the Fermi surface.

phase transitions and other properties of solids [75–77]. With electrostatic control of electron or hole doping, we can tune the location of the Fermi level with no detectable change in the overall band dispersion in these MX monolayers. Considering WC as an example, via employing a self-consistent simulation approach, we reveal that, when moderate doping is introduced, these proposed mono-layers can be switched to the spin valley Hall state, where spin-valley current can be realized. For instance, when the homogeneous charge $\Delta Q = 0.02\ e$ is applied, the Fermi level exactly crosses the conduction band minima decorated with spin-down (spin-up) character at valley K (K'), as shown in figure 13. This allow the spin-valley current in the WC monolayer. As can be recognized from figure 13(d), by further enhancing the doping strength, the Fermi level shifts in the upward direction, but still crossing the lower conduction band. Similarly, by introducing the hole doping with a magnitude of $\Delta Q = -0.025e$, the Fermi level is shifted to the valence band and exactly crosses the valence band minima equipped with in-plane spin-polarized carriers (see figure 13(b)), enabling the spin-polarized transport. With further enhancement of the hole doping, the Fermi level is migrated deep inside the top valence band.

The proposed electric tuning of the spin splitting, by adjusting the doping between electrons and holes, presents possibilities to design the spin-current based devices, such as spin injection or spin-filtering devices, which are highly demandable for boosting and reshaping the spintronic technology. Figure 13 displays the spin device lightly doped with holes. One can observe that only the in-plane spin components cross the Fermi level. Its spin texture can be controlled with gating, and may facilitate the formation of spin devices such as spin-transistor. For spin-transistor, the control of spin procession via external electric field or gate-voltage is essential.

## 12. Alloys of MX monolayers $M_2X_{2-n}Y_n$

Besides the stimuli such as strain and vertical electric field, one of the promising knobs to tune the band gap and spin splitting is mixing different components in materials with different ratios to make alloys. In this context, alloys based on the transition metal dichalcogenides have been synthesized by mixing different transition metals, and chalcogen atoms using various experimental techniques in both bulk and monolayer forms, and consequently have been studied for various properties [78]. Here, by mixing the transition metals (W, Mo) and X (C, Se, S) atoms at different ratios, the ternary alloys labeled as $M_2X_{2-n}Y_n$ can be grown (see figure 14). We prepare a $2 \times 1$ supercell of MX monolayers and then mix the C, S, and Se atoms to make different alloys. We observe that the Fermi surface, band gap, position of conduction band minimum and valence band maximum, and spin splitting can be tuned by modifying the composition of the Se, S, and, C atoms in these MX monolayers. For instance, as can be observed from figure 14, the valence band maxima shifts from *M* point to Γ point in the $W_2SSe$ alloy. Similarly, it shifts to the *S* point in the $Mo_2CS$ alloy. The large non-magnetic Zeeman type and Rashba spin splitting are formed in the outermost/lowermost conduction/valence bands, as can be seen from figure 14. In the case of $Mo_2CS$, the buckling distance is different for those of C and S (see figures 14(a) and (b)). In particular, the vertical distance between the Mo and C is lower as compared to that of Mo and S.

## 13. Interfacial characteristics with type-II band alignment

In below, we shed light on the interfacial characteristics of the MX monolayers by epitaxially growing on different substrates. Typically, the free-standing films of the monolayer systems are not easy to fabricate in experiment, e.g. germanene and stanene are the examples in this context that do not exist in experiments in free-standing forms. In such cases, finding an appropriate substrate becomes essential to grow these monolayers in experiment. In this context, we search prototype substrates for these MX monolayers. Considering WC as a representative example, we theoretically find that MX monolayers can be grown on the top of $WS_2$ and GaTe substrates. The WC can be coupled with $WS_2$ and GaTe substrates via van der Walls interaction with an interlayer equilibrium distance ∼3.05 and 3.21 A, respectively (see figure 15). In our calculation, we adopt the DFT-D3 method of Grimme to incorporate the van der Waals interactions between the WC and $WS_2$ or GaTe systems [79, 80]. The lattice mismatch in our proposed $WC/WS_2$ and WC/GaTe heterostructures are ∼5.3% and 2.90%, respectively. The lattice mismatch seems slightly larger than the typical scale required for the traditional epitaxial growth of two-dimensional materials in the form of heterobilayer. However, due to the presence of moderate van der Waals type interactions instead of strong chemical bonding in these heterbilayers, it is indeed possible to prepare them via the so-called van der Waals epitaxy approaches [81]. Previously, $GaSe/MoSe_2$ (lattice mismatch ∼13%), $Graphene/MoS_2$ (∼28%), and $SnSe_2/MoS_2$ (∼18.7%) heterostructures have been successfully fabricated by utilizing the van der Waals epitaxy strategy [81–83].

From the band structure of $WC/WS_2$ (see figure 15), we can see that this system exhibits the type-II band alignment with the conduction band minimum and valence band maximum existing in the WC and $WS_2$ layers, respectively. The conduction band minimum (at Q point) and valence band maximum (at K point) originate from the *d*-orbitals of WC and $WS_2$, respectively. In such kind of band alignment, electron–hole pairs split at the interface with electrons being assigned to one layer and holes to the other. This allows the formation of photovoltaic devices. For instance, $MoS_2/WS_2$ heterostructure with type-II band-alignment, has been realized as a photovoltaic device that can generate a power conversion with an efficiency ∼1% and considerably higher power-densities than existing ultrathin solar cells [84]. Similarly, such types of hybrid structures can be used to exhibit current rectification and collection of photoexcited carriers [85]. Besides the type-II band alignment, a notable feature associated with these hybrid structures is the large spin splitting around the Fermi level. We observe a spin splitting of ∼215 meV with Zeeman-type in the conduction band minimum, which is much higher than ∼5–30 meV of the pure $WS_2$. And the observed zeeman-type spin splitting in the valence band maximum is ∼405 meV. Furthermore, we also notice a spin splitting of the Rashba-type around Γ point in $WS_2$ system ($\alpha_R \sim 148$ meV Å), which is induced due to the interaction with the WC monolayer (see figure 15(d)). Thus in the $WC/WS_2$ heterobilayer, the larger spin splitting in the conduction band minimum and valence band maximum together with type-II band alignment may have some interesting applications in the field of valleytronics and photonics. These MX monolayers can also be used as an external drive to cause or enlarge Rashba spin splitting by coupling with the materials having limited applications in the spin sector so far due to small Rashba-type spin splitting.

Recently, the experimental realization of $GaSe/MoSe_2$ heterostructure has been reported, which shows that $MoSe_2$ is

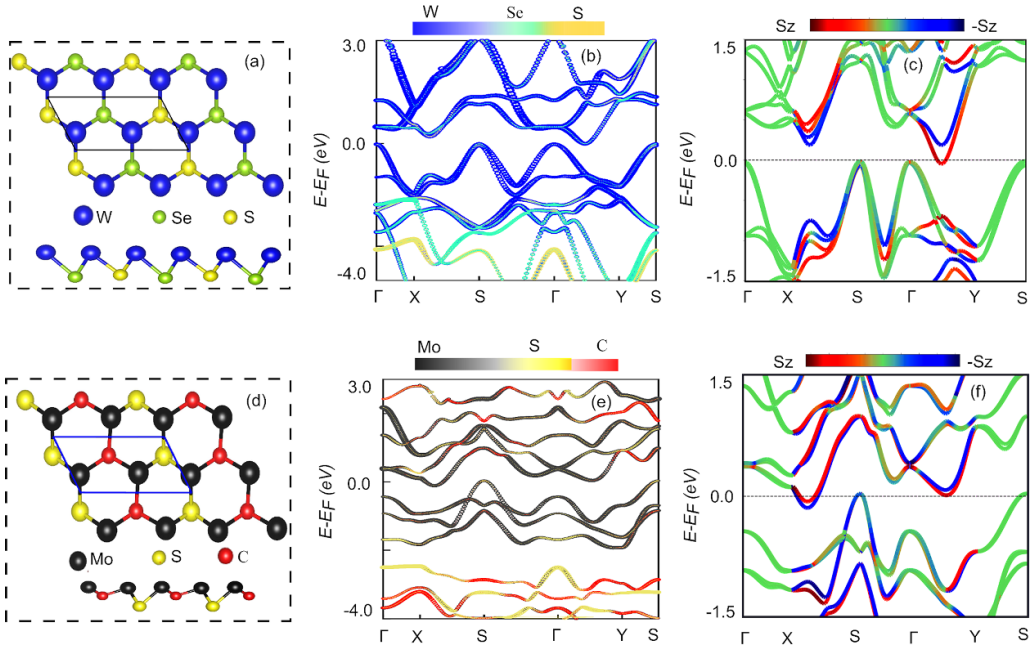


**Figure 14.** Effects on the bandstructure, spin splitting, and position of conduction band minimum and valence band maximum by mixing different X components in the MX monolayers via alloy engineering. (a) Crystal structure of $W_2SSe$ monolayer with both top and side views are shown. (b) Atomic resolved band structure of the $W_2SSe$ in the absence of SOC effects. (c) $S_z$-resolved band structure of the $W_2SSe$ monolayer. The lower panel ((d), (e) and (f)) is for the $Mo_2CS$ monolayer with the same description as stated for the $W_2SSe$ system.

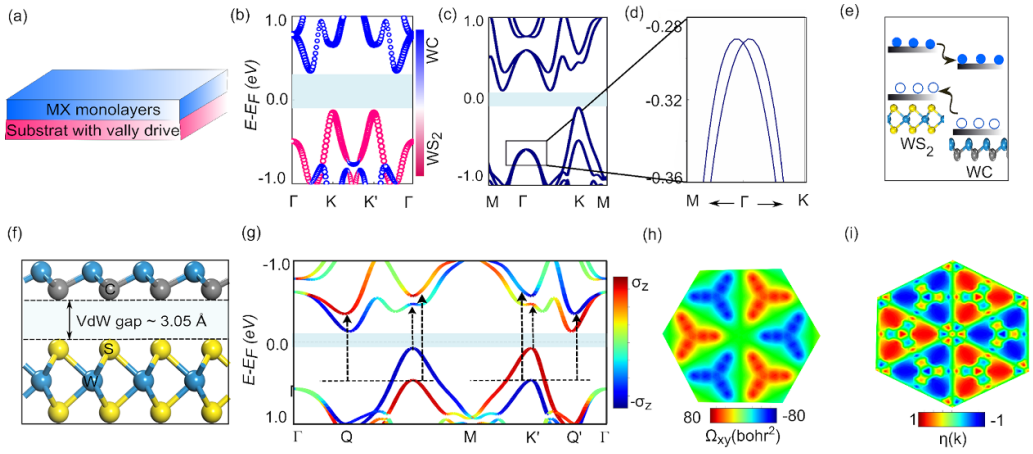


**Figure 15.** Interfacial characteristics of MX monolayers by growing WC layer on the surface of $WS_2$. (a) Schematic representation of MX monolayers over the substrate relevant for the valley transport such as $WS_2$. (b) Layer resolved band structure of WC/$WSe_2$ system without including SOC effect. (c) SOC included band structure of the WC/$WSe_2$ heterobilayer. (d) The zoom-view of the small region around the Γ-point to show more visibly the Rashba effects induced in the substrate due to the WC layer. (e) Schematic representation describing the mechanism of electron and hole splitting in different layers across the interface in the type-II band alignment. (f) Side-view of the atomic geometry of the WC/$WSe_2$ heterobilayer. (g) The $S_z$-resolved band structure of the WC/$WSe_2$ heterobilayer with possible optical transitions are shown. (h) Berry Curvature distribution map in the momentum space; the valley contrasting Berry curvature behavior can be noticed. (i) Valley-driven circular dichroism distribution map where carriers from opposite valleys can be selectively excited by exposing MX monolayers to circularly polarized light.

strongly coupled with GaSe [86]. This indicates that GaTe, which belongs to the same family, can be a good substrate for these MX monolayers. The band structure of WC/GaTe (figure 16(c)) confirms that it demonstrates a type-II band alignment, where the conduction band minimum and valence band maximum exist in the WC and GaTe layers, respectively.

## 14. An efficient source for exploiting spin splitting in other systems

It has been theoretically reported that when SOC combine with other degrees of freedom such as valley, circularly polarized light and magnetism in Xene solids, it gives a spectrum of phenomena ranging from quantum spin Hall to quantum

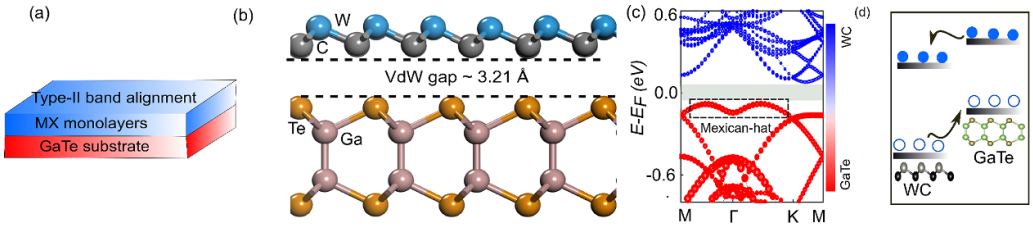


**Figure 16.** Interfacial characteristics of MX monolayers by growing WC on the surface of GaTe. (a) Schematic sketch of the MX monolayers over the GaTe substrate. (b) Crystal structure of WC/GaTe heterostructure. (c) Free-SOC layered resolved band structure of the WC/GaTe system with conduction band minimum and valence band maximum corresponds to different layers signifying the type-II band alignment. (d) Schematic representation explaining the carrier splitting across the interface in the type-II band alignment.

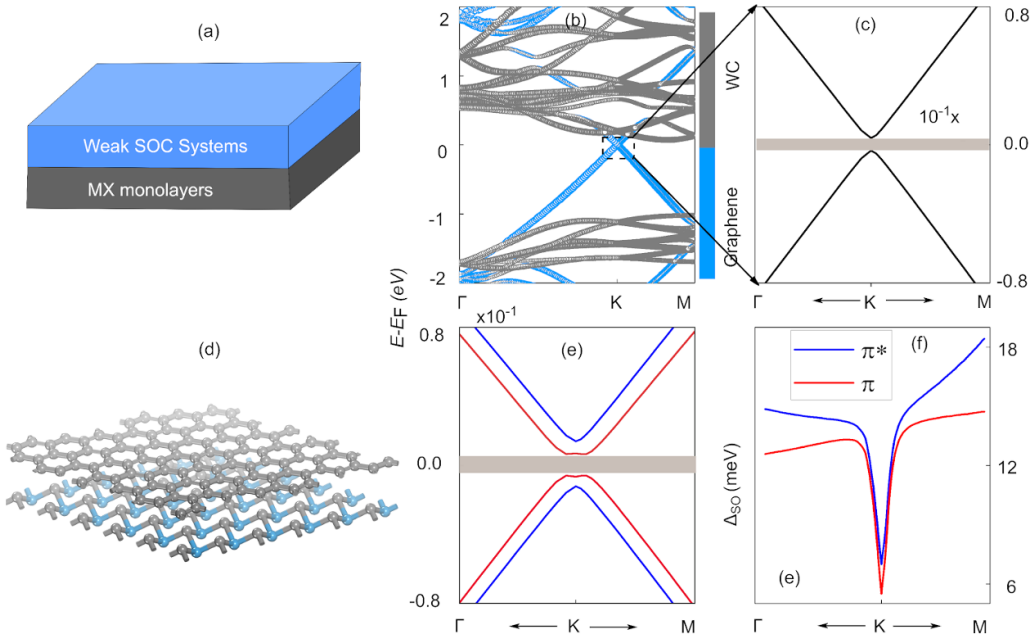


**Figure 17.** (a) Schematic representation to intensify the SO interaction in systems having weak SOC effects such as graphene by coupling with MX films. The top and side view of the geometrical structure of graphene/CW system is also shown. (b) Layered resolved electronic band structure of the graphene/CW system with the graphene states are residing within the bandgap of the CW. (c) Zoom view of the region around the valley $K$-point. (d) The top view of the geometrical structure of graphene/CW system. (e) Electronic band structure of the graphene/CW system in the presence of SO coupling where the high spin splitting of the conduction and valence bands can be observed. (f) Momentum dependent variation of the spin splitting in the topmost valence $\pi$ and lowermost conduction $\pi^*$ bands.

valley Hall effect [4, 87, 88]. However, due to insufficient SOC in Xene solids, the practical realization of these phenomena is challenging. In this context, we ask a question: can these MX monolayers be used to enhance the SOC in Xene solids with weak SOC? To answer this question, we grow the graphene layer over the WC monolayer as a prototype example. Although, there are various previous reports which show that SOC can be induced in graphene via interfacial coupling with systems having strong SOC [89–91]. However, specific studies where proximity effects are interface dependent, have rarely discussed and still lie within the scope of the current research. In this context, the study focusing on the graphene system coupled with the MX layers can be interesting because proximity effects in graphene over WC monolayer may be strongly dependent on the surface morphology of WC monolayer. In principle, the WC monolayer has two distinct surfaces and can establish two different types of interfacial interaction with a graphene sheet. We find that graphene can be epitaxially grown on these MX monolayers. For instance, graphene can be deposited on WC with a small lattice mismatch around $\sim$1.8% (see figures 17(c) and (d)). Due to two distinct surfaces of the WC monolayer, the graphene sheet can pair up with either C-layer or the W-layer of the WC sheet. We symbolize the growth of graphene over the WC monolayer by graphene/CW, when the C-layer in the WC sheet is close to the graphene sheet (see figure 17(d)). While it is denoted by graphene/WC when the W-layer is close to the graphene sheet (see figure 18(b)). First, we shed light on the graphene/CW heterobilayer when C-layer of WC is near the graphene sheet (see figure 17(d)). The interlayer distance between graphene and CW monolayers is around 2.87 Å, showing moderate coupling between these two systems. In the band structure of graphene/CW as shown in figure 17, we can see that the graphene states are located in the bulk band gap of CW. After coupling with CW, graphene $p_z$ orbital is coupled to the substrate, which converts the massless Dirac

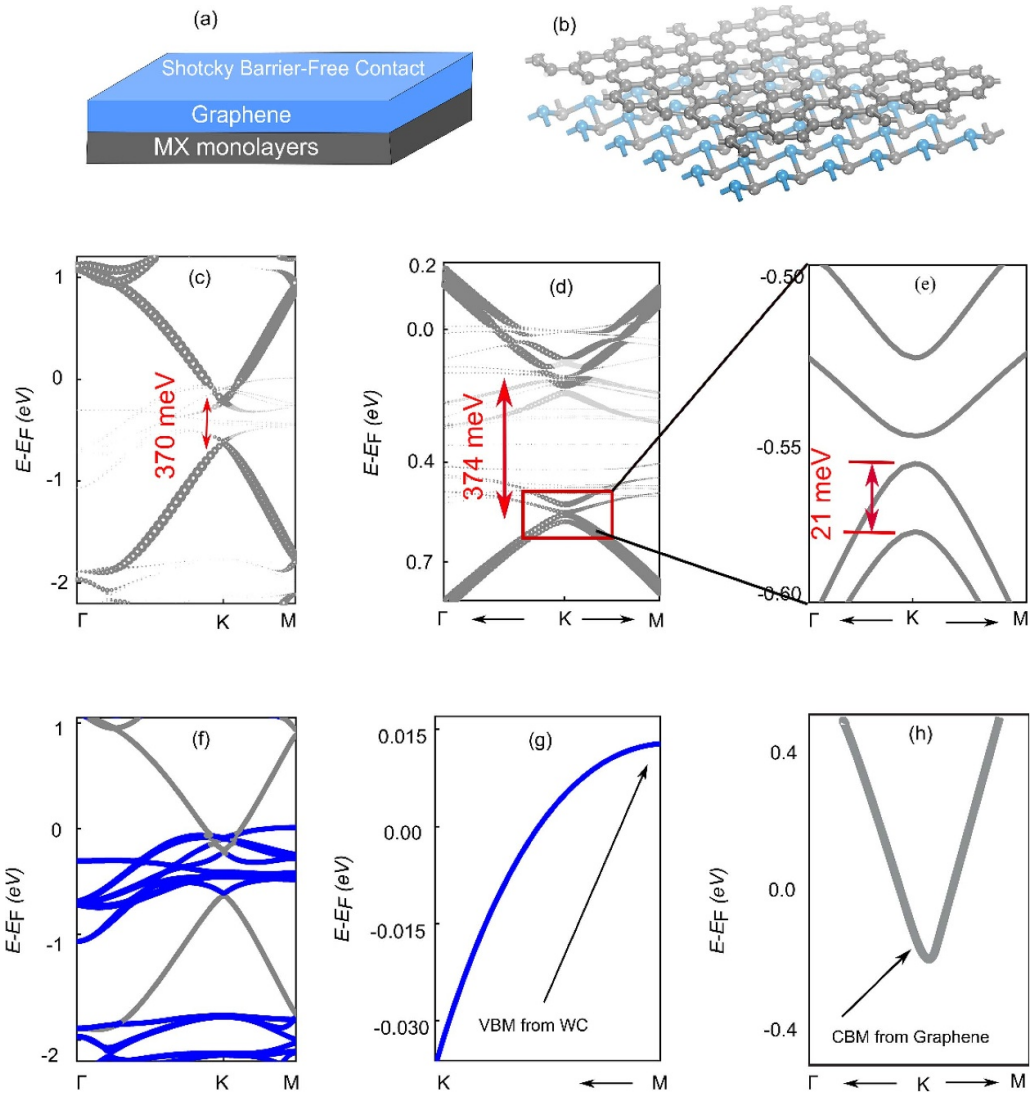


**Figure 18.** (a) Schematic representation by growing the graphene layer over the WC system. Geometrical structure in the top view (b) and side-view (C) of the graphene/WC system. (d) The SOC-free electronic bandstructure of the graphene/WC system where the states are projected over the graphene layer. (e) The electronic bandstructure projected over the graphene layer in the presence of SOC effect where the high spin splitting in the valence and conduction bands of graphene can be observed, indicating the strong induction of SOC in the graphene layer. (g) SOC-free band structure projected over the WC layer. (h) Topmost valence band of the WC layer in the graphene/WC system. Lowermost conduction band of the graphene in the graphene/WC system. From (g) and (h), it can be perceived that the valence band of the WC is higher in energy than the conduction band of the graphene layer, pointing toward the formation of the Schtocky barrier-free contact.

cone of graphene into a massive one with a direct band gap ∼7.2 meV (see figure 17(b)). This band gap originates from the staggered potential induced by the substrate. When incorporating the SOC effect, not only do the band gaps at $K$ and $K'$ points increase (∼12.4 meV), but also we observe a spin splitting in the $\pi$ and $\pi^*$ bands of graphene (see figures 17(c) and (d)). The enhancement of the bandgap and the induced spin-slitting indicate that MX monolayers are indeed capable of strengthening the SOC effects in graphene. Such kind of behavior has been reported for graphene grown over the transition metal dichalcogenides [92] and $n-p$ codoped graphene system [93]. The spin splitting in the $\pi$ and $\pi^*$ bands may arise from the combined effects of the vertical electric field, intrinsic SOC and Rashba SOC. The variation of the spin splitting size in the vicinity of K point in the $\pi$ and $\pi^*$ bands is shown in figure 17(f). The size of the spin splitting intensifies as we move away from the valley point. For instance, the spin splitting of $\pi$ band at K is ∼6 meV, which increases to ∼19 meV, when it moves away from K toward M. These values are comparable to the previous studies where graphene was deposited over several systems to induce SOC effects [89–91].

Next, we consider the situation when the W-layer of the WC monolayer is near the graphene sheet (i.e. graphene/WC). Overall, the graphene/WC heterobilayer is metallic and has no global band gap. The Fermi level crosses the conduction band, indicating that it is electron-doped. As shown in figure 18, the conduction and valence bands of graphene are separated by a wide energy gap of 370 meV. Indeed, from the spin splitting perspective, the graphene/WC system is more effective than graphene/CW configuration, which can be observed

from figures 18(e) and (f). In particular, the conduction band of graphene splits 81 meV, whereas the valence band splits around 21 meV, showing an intense penetration of spin effects in graphene from WC monolayer. Thus the MX monolayers can induce strong SOC effects in the systems with weak SOC.

Many theoretical proposals, extending from the substitutional doping to surface adsorption mechanism, have been made to enhance SOC effects in graphene [4, 94]. However, up to date, no experimental evidence has been reported for these proposals, due to the possible reasons of difficult control of adatom concentration (such as clustering formation) or weak electrostatic coupling between adatoms and graphene. Enhancing SOC effects in graphene via substrate is farther better than by using the adsorption or doping strategy.

## 15. Shtocky barrier-free contact by coupling with other systems

Now, we focus on the van der Waals contacted metal-semiconductor junction between graphene and WC. Metal-semiconductor junction plays a significant role in a field-effect transistor, whose the performance largely depends on the resistance across the junction, that is, the so-called Schottky barrier. In contrast to traditional junctions, van der Waals contacted metal-semiconductor junctions can overwhelm the effect of Fermi level pinning [95, 96]. And thereby achieving tunable Schottky barrier and even with vanishing resistance, when proper two-dimensional systems are coupled. For van der Waals contacted metal-semiconductor junctions, the Schottky barrier is parameterized by $\Phi_e/\Phi_h$ (height for electron/hole injection), which is defined as $\Phi_e = E_{CBM} - E_F$; $\Phi_h = E_F - E_{VBM}$. Here, $E_F$ represents the Fermi level of metal, and $E_{VBM}$ ($E_{CBM}$) correspond to the energy of valence band maximum (conduction band minimum) of the semiconductor. The performance of metal-semiconductor junctions depends on the degree of $\Phi_e$ (or $\Phi_h$); the smaller $\Phi_e$ (or $\Phi_h$), the better the metal-semiconductor junction. It can be seen from figures 18(h) and (i), the conduction band of graphene becomes lower than the valence band of WC. This points toward the potentiality where electrons in the valence band of WC can transfer to the graphene conduction band (figures 18(h) and (i)), suggesting that Schottky barrier-free contact can be formed for hole injection in graphene/WC heterobilayer.

## 16. Conclusion

Employing the fully relativistic calculations based on density functional theory, we explore a family of solid materials that are based on transition metals with MX chemical composition. This MX family presents a large and electrically switchable anisotropic Rashba-like and non-magnetic Zeeman-type spin splittings. Our analysis shows these large spin splittings appear due to the following three ingredients that exist intrinsically in these MX monolayers: (i) Broken out-of-plane mirror-symmetry with large out-of-plane spontaneous polarization; (ii) sizable SOC; and (iii) similar atomic and orbital features around the Fermi level. We find that the spin splitting in these MX monolayers can be further tuned by external means such as subjecting to symmetrical/asymmetric strain, vertical electric field and alloy engineering. In particular, it is possible to enhance the amplitude of the Rashba interaction with the application of positive electric field or epitaxial growing these monolayers on the substrate with compressive strain. On the other side, the strength of Rashba SOC becomes weaker in these MX monolayers by exposing them to negative electric field or stretching these monolayers.

Additionally, we establish a connection between the lattice distortion and Rashba spin splitting by applying a uniaxial strain along the zigzag direction. With the application of this asymmetrical strain, not only does the Rashba spin splitting in the top valence band enhances, but also the lower conduction bands become spin-splitted around the $\Gamma$ point, indicating a strong link between the lattice and spin splitting in these MX monolayers. This can be used as a new pathway to optimize and control the strength of Rashba interaction through the subtle interplay between lattice and electronic degrees of freedom appearing in these MX systems. Interestingly, we also mark significant anisotropic energy spin splitting $\Delta E_R$ along the $\Gamma \rightarrow K$ and $\Gamma \rightarrow M$ directions, which can be used to furnish the spin-polarized spin channels at the Fermi surface of these monolayers, allowing the formation of spin devices (spin injection or spin filter devices). Furthermore, the size of the Zeeman spin splitting in the conduction band minimum is observed to be in the range of 120–465 meV for MX systems, which is notably high as compared to the two-dimensional transition metal dichalcogenides ($WSe_2$, $WS_2$, and $MoSe_2$).

We notice the valley contrasting Berry curvature behavior in the MX monolayers, where the finite but opposite Berry curvatures originate from the opposite valleys. Due to opposite Berry curvatures from the two valleys together with non-zero global band gap, these MX monolayers are intrinsic quantum valley Hall insulators. The carriers from the two valleys can be selectively excited using the circularly polarized light as a stimulation. These MX monolayers give topological responses with robust helical edge states when grown in the form of paraelectric geometry. It can be used as a spin modulator source for other systems with weak SOC effects such as graphene. Furthermore, depending on the stacking patterns, graphene deposited over the graphene sheet passes through the transformation from the semiconducting junction to the Shotcky barrier-free contact. These MX monolayers could also be grown on the substrates such as $WS_2$(001) and GaTe (001) with type-II band alignment, where electron and hole become layer splitting across the interface. Our analysis should be fairly applicable to other systems existing in the same geometry, such as WN, TaN, ZrTe, MoP, MoN, NbN, and NbS.

Recently, the emergence of spin degrees of freedom is also realized in the cross fields such as electrochemistry where usually the spin degree of freedom is ignored [97–99]. For instance, by introducing spin degrees freedom, conventional electrochemistry can evolve into spin electrochemistry with various useful applications [97–99]. The coupling of spin with orbital degrees of freedom (i.e. the SOC) in heavy

metal oxides can cause *d*-band splitting thus generates spin-polarized currents.

Our study could establish an valuable platform for both conventional and topological spintronics applications based on anisotropic Rashba-like and non-magnetic Zeeman-type spin splitting with tunable nature.

## Data availability statement

All data that support the findings of this study are included within the article (and any supplementary files).

## Acknowledgments

This work was financially supported by the National Natural Science Foundation of China (Grant Nos. 11974327 and 12004369), Fundamental Research Funds for the Central Universities (WK3510000010, WK2030020032), Anhui Initiative in Quantum Information Technologies (Grant No. AHY170000). We also thank the supercomputing service of AM-HPC and the Supercomputing Center of University of Science and Technology of China for providing the high performance computing resources.

## ORCID iD

Zhenhua Qiao https://orcid.org/0000-0003-2792-5110

## References

[1] Chappert C, Fert A and VanDau F N 2007 *Nat. Mater.* **6** 813
[2] Manipatruni S, Nikonov D E, Ramesh R, Li H and Young I A arXiv:1512.05428v2
[3] Soumyanarayanan A, Reyren N, Fert A and Panagopoulos C 2016 *Nature* **539** 509
[4] Ren Y, Qiao Z and Niu Q 2016 *Rep. Prog. Phys.* **79** 066501
[5] Rehman M U, Dong X, Hou T, Li Z, Qi S and Qiao Z 2019 *Phys. Rev.* B **100** 195422
[6] Rehman M U 2018 *Physica* B **547** 72
[7] Rehman M U, Qiao Z and Wang J 2022 *Phys. Rev.* B **105** 165417
[8] Kato Y K, Myers R C, Gossard A C and Awschalom D D 2004 *Science* **306** 1910
[9] Zhao H, Loren E J, van Driel H M and Smirl A L 2006 *Phys. Rev. Lett.* **96** 246601
[10] Ando K and Saitoh E 2012 *Nat. Commun.* **3** 629
[11] Bychkov Y A and Rashba E I 1984 *JETP Lett.* **39** 78 (available at: http://jetpletters.ru/ps/1264/article_19121.shtml)
[12] Bihlmayer G, Rader O and Winkler R 2015 *New J. Phys.* **17** 050202
[13] Stranks S D and Plochocka P 2018 *Nat. Mater.* **17** 377
[14] Manchon A, Koo H C, Nitta J, Frolov S M and Duine R A 2015 *Nat. Mater.* **14** 871
[15] Varignon J, Vila L, Barthmy A and Bibes M 2018 *Nat. Phys.* **14** 322
[16] Bihlmayer G, Noel P and Vyalikh D V 2022 *Nat. Rev. Phys.* **3** 1296
[17] Min H, Hill J E, Sinitsyn N A, Sahu B R, Kleinman L and MacDonald A H 2006 *Phys. Rev.* B **74** 165310
[18] Konschuh S, Gmitra M and Fabian J 2010 *Phys. Rev.* B **82** 245412
[19] Liu Q, Guo Y and Freeman A J 2013 *Nano Lett.* **13** 5264
[20] Lee K, Yun W S and Lee J D 2015 *Phys. Rev.* B **91** 125420
[21] Arras R, Gosteau J, Zhao H J, Paillard C, Yang Y and Bellaiche L 2019 *Phys. Rev.* B **100** 174415
[22] Varignon J, Santamaria J and Bibes M 2019 *Phys. Rev. Lett.* **122** 116401
[23] Hu T, Jia F, Zhao G, Wu J, Stroppa A and Ren W 2018 *Phys. Rev.* B **97** 235404
[24] Ma Y, Kou L, Huang B, Dai Y and Heine T 2018 *Phys. Rev.* B **98** 085420
[25] Singh S and Romero A H 2017 *Phys. Rev.* B **95** 165444
[26] Zhang Q and Schwingenschlogl U 2018 *Phys. Rev.* B **97** 155415
[27] Sante D D, Stroppa A, Barone P, Whangbo M and Picozzi S 2015 *Phys. Rev.* B **91** 161401(R)
[28] Cheng Y C, Zhu Z Y, Tahir M and Schwingenschlogl U 2013 *Europhys. Lett.* **102** 57001
[29] Hussain G, Samad A, Rehman M U, Cuono G and Autieri C 2022 *J. Mag. Mag. Mater.* **563** 169897
[30] Rehman M U, Kiani M and Wang J 2022 *Phys. Rev.* B **105** 195439
[31] Ishizaka K, Bahramy M S and Murakawa H 2011 *Nat. Mater.* **10** 521
[32] LaShell S, McDougall B A and Jensen E 1996 *Phys. Rev. Lett.* **77** 3419
[33] Koroteev Y M, Bihlmayer G, Gayone J E, Chulkov E V, Blügel S, Echenique P M and Hofmann P 2004 *Phys. Rev. Lett.* **93** 046403
[34] Ast C R, Henk J, Ernst A, Moreschini L, Falub M C, Pacilé D, Bruno P, Kern K and Grioni M 2007 *Phys. Rev. Lett.* **98** 186807
[35] Kimura A, Krasovskii E E, Nishimura R and Miyamoto K 2010 *Phys. Rev. Lett.* **105** 076804
[36] Nitta J, Akazaki T, Takayanagi H and Enoki T 1997 *Phys. Rev. Lett.* **78** 1335
[37] Zutic I, Fabian J and Das Sarma S 2004 *Rev. Mod. Phys.* **76** 323
[38] Yuan H *et al* 2013 *Nat. Phys.* **9** 563
[39] Xiao D, Liu G, Feng W, Xu X and Yao W 2012 *Phys. Rev. Lett.* **108** 196802
[40] Liu Q, Zhang X, Jin H, Lam K, Im J, Freeman A and Zunger A 2015 *Phys. Rev.* B **91** 235204
[41] Zhu Z, Winkler G W, Wu Q, Li J and Soluyanov A A 2016 *Phys. Rev.* X **6** 031003
[42] Singh S, Wu Q, Yue C, Romero A H and Soluyanov A A 2018 *Phys. Rev. Mater.* **2** 114204
[43] Clougherty E V, Lothrop K H and Kafalas J A 1961 *Nature* **191** 1194
[44] Pasquazzi A, Schubert W D, Halwax E and Kremser G 2013 *Proc. 18th Plansee Seminar* (available at: https://publik.tuwien.ac.at/files/PubDat_222121.pdf)
[45] Lalmi B, Oughaddou H, Enriquez H, Kara A, Vizzini S, Ealet B and Aufray B 2010 *Appl. Phys. Lett.* **97** 223109
[46] Feng B, Ding Z, Meng S, Yao Y, He X, Cheng P, Chen L and Wu K 2012 *Nano Lett.* **12** 3507
[47] Sone J, Yamagami T, Aoki Y, Nakatsuji K and Hirayama H 2014 *New J. Phys.* **16** 095004
[48] Li L, Lu S, Pan J, Qin Z, Wang Y-Q, Wang Y, Cao G-Y, Du S and Gao H-J 2014 *Adv. Mater.* **26** 4820
[49] Kresse G and Hafner J 1993 *Phys. Rev.* B **47** 558
[50] Kresse G and Furthmuller J 1996 *Comput. Mater. Sci.* **6** 15
[51] Blochl P E 1994 *Phys. Rev.* B **50** 17953
[52] Perdew J P, Burke K and Ernzerhof M 1996 *Phys. Rev. Lett.* **77** 3865
[53] Bengtsson L 1999 *Phys. Rev.* B **59** 12301
[54] Heyd J, Scuseria G E and Ernzerhof M 2003 *J. Chem. Phys.* **118** 18
[55] Baroni S, de Gironcoli S, Dal Corso A and Giannozzi P 2001 *Rev. Mod. Phys.* **73** 515
[56] Togo A and Tanaka I 2015 *Scr. Mater.* **108** 1

[57] Mostofi A A, Yates J R, Lee Y-S, Souza I, Vanderbilt D and Marzari N 2008 *Comput. Phys. Commun.* **178** 685
[58] Pizzi G, Vitale V, Arita R, Blugel S, Freimuth F, Geranton G, Gibertini M, Gresch D, Johnson C and Koretsune T 2020 *J. Phys.: Condens. Matter* **32** 165902
[59] Wu Q, Zhang S, Song H-F Troyer M and Soluyanov A A 2018 *Comput. Phys. Commun.* **224** 405
[60] Herath U, Tavadze P, He X, Bousquet E, Singh S, Muñoz F and Romero A H 2020 *Comput. Phys. Commun.* **251** 107080
[61] Samad A, Kim H J and Shin Y 2019 *J. Phys.: Condens. Matter* **31** 045301
[62] Cheng C, Sun J, Chen X, Fua H and Meng S 2016 *Nanoscale* **8** 17854
[63] Huang S M, Badrutdinov A O, Serra L, Kodera T, Nakaoka T, Kumagai N, Arakawa Y, Tayurskii D A, Kono K and Ono K 2011 *Phys. Rev.* **B84** 085325
[64] Nitta J, Akazaki T, Takayanagi H and Enoki T 1997 *Phys. Rev. Lett.* **78** 1335
[65] LaShell S, McDougall B A and Jensen E 1996 *Phys. Rev. Lett.* **77** 3419
[66] Koroteev Y M, Bihlmayer G, Gayone J E, Chulkov E V, Blügel S, Echenique P M and Hofmann P 2004 *Phys. Rev. Lett.* **93** 046403
[67] Oh S and Choi H J 2017 *Sci. Rep.* **7** 2024
[68] Szary M J, Michalewicz M T and Radny M W 2019 *Appl. Surf. Sci.* **494** 619
[69] Park S R, Kim C H, Yu J, Han J H and Kim C 2011 *Phys. Rev. Lett.* **107** 156803
[70] Kim B, Kim C H and Kim P 2012 *Phys. Rev.* B **85** 195402
[71] Park S R *et al* 2012 *Phys. Rev. Lett.* **108** 046805
[72] Kim B *et al* 2013 *Phys. Rev.* B **88** 205408
[73] Pan H, Li X, Qiao Z, Liu C-C, Yao Y and Yang S A 2014 *New J. Phys.* **16** 123015
[74] Szary M J 2019 *Appl. Surf. Sci.* **491** 469
[75] Saito Y, Nojima T and Iwasa Y 2016 *Nat. Rev. Mater.* **2** 16094
[76] Nguyen P V *et al* 2019 *Nature* **572** 220
[77] Sun Z, Sun Z, Martinez A and Wang F 2016 *Nat. Photon.* **10** 227
[78] Xie L M 2015 *Nanoscale* **7** 18392
[79] Grimme S 2006 *J. Comput. Chem.* **27** 1787
[80] Grimme S, Antony J, Ehrlich S and Krieg H 2010 *J. Chem. Phys.* **132** 154104
[81] Li X *et al* 2016 *Sci. Adv.* **2** 1501882
[82] Shi Y *et al* 2012 *Nano Lett.* **12** 2784
[83] Zhao M, Liu M, Dong Y, Zou C, Yang K, Yang Y, Zhang L and Huang S 2016 *J. Mater. Chem.* C **4** 10215
[84] Bernardi M, Palummo M and Grossman J C 2013 *Nano Lett.* **13** 3664
[85] Lee C-H *et al* 2014 *Nat. Nanotechnol.* **9** 676
[86] Li X, Lin M-W and Lin J 2016 *Sci. Adv.* **2** e150188
[87] Rehman M U and Qiao Z 2018 *Eur. Phys. J.* B **91** 42
[88] Rehman M U and Abid A A 2017 *Chin. Phys.* B **26** 127304
[89] Lee P *et al* 2015 *ACS Nano* **9** 10861
[90] Avsar A *et al* 2014 *Nat. Commun.* **5** 4875
[91] Frank T, Gmitra M and Fabian J 2016 *Phys. Rev.* B **93** 155142
[92] Wakamura T, Reale F, Palczynski P, Zhao M Q, Johnson A T C, Guéron S, Mattevi C, Ouerghi A and Bouchiat H 2019 *Phys. Rev.* B **99** 245402
[93] Qi S, Han Y, Xu F, Xu X and Qiao Z 2019 *Phys. Rev.* B **99** 195439
[94] Jiang H, Qiao Z, Liu H, Shi J and Niu Q 2012 *Phys. Rev.* B **109** 116803
[95] Liu Y, Guo J, Zhu E, Liao L, Lee S-J , Ding M, Shakir I, Gambin V, Huang Y and Duan X 2018 *Nature* **557** 696
[96] Liu Y, Stradins P and Wei S-H 2016 *Sci. Adv.* **2** e1600069
[97] Li J, Ma J, Ma Z, Zhao E, Du K, Guo J and Ling T 2021 *Adv. Energy Sustain. Res.* **2** 2100034
[98] Chen R R, Chen G, Ren X, Ge J, Ong S J H, Xi S, Wang X and Xu Z J 2021 *Angew. Chem., Int. Ed.* **60** 25884
[99] Chen G, Sun Y, Chen R R, Biz C, Fisher A C, Sherburne M P, Ager III J W, Gracia J and Xu Z J 2021 *J. Phys. Energy* **3** 031004